Monthly Notices
of the
ROYAL ASTRONOMICAL SOCIETY

MNRAS **434,** 3104–3121 (2013) doi:10.1093/mnras/stt1228
Advance Access publication 2013 July 29

A quasar–galaxy mixing diagram: quasar spectral energy distribution shapes in the optical to near-infrared

Heng Hao,[1,2]★ Martin Elvis,[2] Angela Bongiorno,[3,4] Gianni Zamorani,[5] Andrea Merloni,[3] Brandon C. Kelly,[6] Francesca Civano,[2,7] Annalisa Celotti,[1,8] Luis C. Ho,[9] Knud Jahnke,[10] Andrea Comastri,[5] Jonathan R. Trump,[11] Vincenzo Mainieri,[12] Mara Salvato,[13,14] Marcella Brusa,[3,15] Chris D. Impey,[16] Anton M. Koekemoer,[17] Giorgio Lanzuisi,[3] Cristian Vignali,[5,15] John D. Silverman,[18] C. Megan Urry[19] and Kevin Schawinski[20]

[1]*SISSA, Via Bonomea 265, I-34136 Trieste, Italy*
[2]*Harvard–Smithsonian Center for Astrophysics, 60 Garden Street, Cambridge, MA 02138, USA*
[3]*Max Planck Institute für Extraterrestrische Physik, Postfach 1312, D-85741 Garching bei München, Germany*
[4]*INAF – Osservatorio Astronomico di Roma, Via di Frascati 33, I-00040 Monteporzio Catone, Rome, Italy*
[5]*INAF – Osservatorio Astronomico di Bologna, via Ranzani 1, I-40127 Bologna, Italy*
[6]*Department of Physics, Broida Hall, University of California, Santa Barbara, CA 93106, USA*
[7]*Department of Physics and Astronomy, Dartmouth College, 6127 Wilder Lab, Hanover, NH 03755, USA*
[8]*INAF – Osservatorio Astronomico di Brera, via E. Bianchi 46, I-23807 Merate, Italy*
[9]*The Observatories of the Carnegie Institute for Science, Santa Barbara Street, Pasadena, CA 91101, USA*
[10]*Max-Planck-Institut für Astronomie, Königstuhl 17, D-69117 Heidelberg, Germany*
[11]*UCO/Lick Observatory, University of California, Santa Cruz, CA 95064, USA*
[12]*European Southern Observatory, Karl-Schwarzschild-Strasse 2, D-85748 Garching bei München, Germany*
[13]*IPP – Max-Planck-Institute for Plasma Physics, Boltzmann Strasse 2, D-85748 Garching bei München, Germany*
[14]*Excellence Cluster, Boltzmann Strasse 2, D-85748 Garching bei München, Germany*
[15]*Dipartimento di Fisica e Astronomia, Università degli studi di Bologna, viale Berti Pichat 6/2 I-40127 Bologna, Italy*
[16]*Steward Observatory, University of Arizona, 933 North Cherry Avenue, Tucson, AZ 85721, USA*
[17]*Space Telescope Science Institute, 3700 San Martin Drive, Baltimore, MD 21218, USA*
[18]*Kavli Institute for the Physics and Mathematics of the Universe, Todai Institutes for Advanced Study, the University of Tokyo, Kashiwa 277-8583, Japan (Kavli IPMU, WPI)*
[19]*Physics Department and Yale Center for Astronomy and Astrophysics, Yale University, New Haven, CT 06511, USA*
[20]*Institute for Astronomy, Department of Physics, ETH Zurich, Wolfgang-Pauli-Strasse 16, CH-8093 Zurich, Switzerland*

Accepted 2013 July 2. Received 2013 July 1; in original form 2012 October 10

ABSTRACT

We define a quasar–galaxy mixing diagram using the slopes of their spectral energy distributions (SEDs) from 1 μm to 3000 Å and from 1 to 3 μm in the rest frame. The mixing diagram can easily distinguish among quasar-dominated, galaxy-dominated and reddening-dominated SED shapes. By studying the position of the 413 *XMM*-selected type 1 AGN in the wide-field 'Cosmic Evolution Survey' in the mixing diagram, we find that a combination of the Elvis et al. mean quasar SED with various contributions from galaxy emission and some dust reddening is remarkably effective in describing the SED shape from 0.3 to 3 μm for large ranges of redshift, luminosity, black hole mass and Eddington ratio of type 1 AGN. In particular, the location in the mixing diagram of the highest luminosity AGN is very close (within 1σ) to that of the Elvis et al. SED template. The mixing diagram can also be used to estimate the host galaxy fraction and reddening in quasar. We also show examples of some outliers which might be AGN in different evolutionary stages compared to the majority of AGN in the quasar–host galaxy co-evolution cycle.

Key words: surveys – galaxies: evolution – quasars: general.

★E-mail: henghao@post.harvard.edu

1 INTRODUCTION

The masses of the supermassive black holes (SMBHs) that exist in most, if not all, galaxy nuclei (e.g. Kormendy & Richstone 1995), are proportional to their host galaxy bulge stellar mass, as measured by either luminosity (Kormendy & Richstone 1995; Marconi & Hunt 2003) or velocity dispersion (Ferrarese & Merritt 2000; Gebhardt et al. 2000). As most SMBH growth occurs during their active phases (the 'Soltan argument', Soltan 1982), most bulges must have gone through an active phase, being seen as a quasar or active galactic nucleus (AGN). It is observed that both galaxies and AGN exhibit coordinated 'downsizing': massive galaxy star formation peaks at $z \sim 2$, while high-luminosity quasars have their peak space density at $z = 2$–3 (Silverman et al. 2005; Brusa et al. 2010; Civano et al. 2011); lower mass galaxies star formation peaks at $z = 1$–1.5, as do lower luminosity AGN (Franceschini et al. 1999; Ueda et al. 2003; Brandt & Hasinger 2005; Bongiorno et al. 2007). A close co-evolutionary link between SMBH activity and host galaxy evolution seems to be required.

In principle, we could study whatever feedback process controls this co-evolution, by separately analysing the emission associated with the SMBH and the host galaxy in the same objects. Observationally, however, it is difficult to disentangle the emission from quasar and host galaxy in the optical–infrared range, especially for high-redshift ($z > 1$) objects. Spatially decomposing a point source AGN and an extended host requires expensive high-resolution *Hubble Space Telescope* (*HST*) imaging. Even the 0.1 arcsec angular resolution of the Hubble cannot easily resolve the extended host emission from the point-like AGN emission at $z > 1$ (e.g. Cisternas et al. 2011). Spectral energy distribution (SED) fitting techniques can do so, but have to assume one or several quasar and galaxy SED models (e.g. Merloni et al. 2010), which might lead to systematic errors that are difficult to quantify.

As an alternative approach, we have made use of the fact that the SEDs of a quasar and of a galaxy near 1 μm are completely different. Quasar SEDs show a pronounced dip near 1 μm (e.g. Elvis et al. 1994, E94 hereinafter; Richards et al. 2006, R06 hereinafter), while, in contrast, a galaxy SED peaks at around 1–2 μm. This dichotomy allows us to define a diagram of near-infrared (NIR) versus optical (OPT) slopes on either side of 1 μm (rest frame) that cleanly separates the two SED forms.

In this diagram (Fig. 1), galaxies lie in a well-defined region ($\alpha_{\rm OPT} < 0, \alpha_{\rm NIR} > 0.8$), that is clearly distinct from the location of the standard AGN SED ($\alpha_{\rm OPT} > 0$, $\alpha_{\rm NIR} < 0$; E94). Reddening moves objects almost perpendicularly to a line joining the galaxy locus to the AGN locus in the diagram. Thus, this diagram can distinguish the quasar-dominated, host-dominated or reddening-dominated SEDs easily, without strong model assumptions, and can pick out AGN with mixtures of these three components. Hence, we call this the

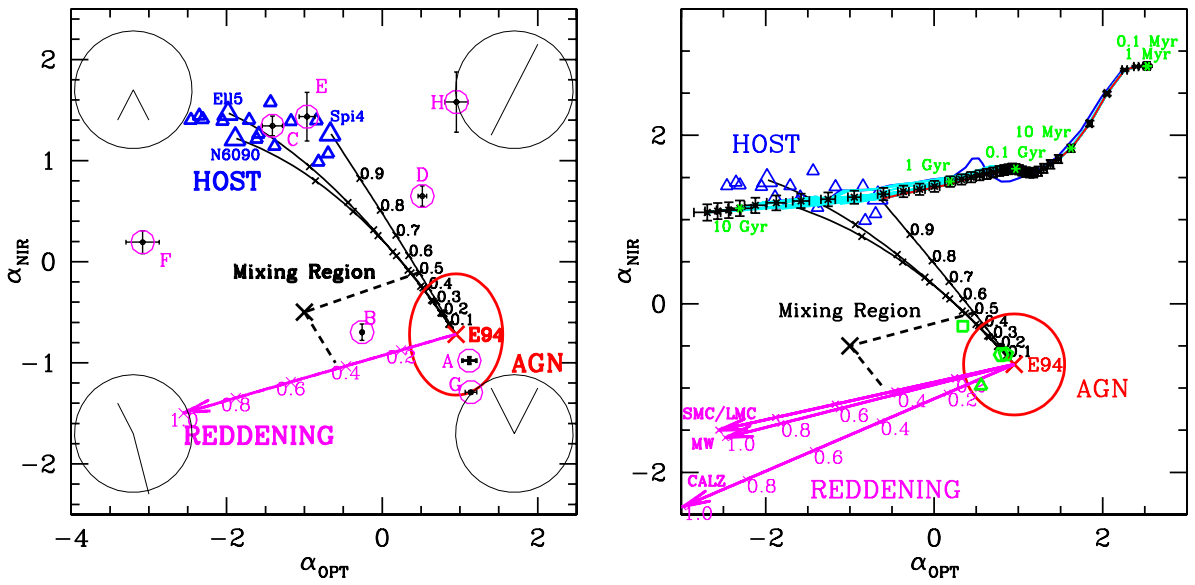

Figure 1. Two representations of the quasar–galaxy mixing diagram, $\alpha_{\rm NIR}$ (3–1 μm) versus $\alpha_{\rm OPT}$ (1–0.3 μm). Note that these slopes are defined in the $\log\nu L_\nu$ versus $\log\nu$ plane. The E94 radio-quiet mean SED is shown as a red cross ($\alpha_{\rm OPT} = 0.95 \pm 0.04$ and $\alpha_{\rm NIR} = -0.72 \pm 0.05$). The red circle shows the dispersion of the quasar samples (Section 3.3). The blue triangles indicate the 16 galaxy templates from 'SWIRE template library' (Polletta et al. 2007). The black lines connecting the SWIRE galaxy templates and the E94 mean SED are mixing curves (Section 2.3), showing where mixed quasar–galaxy SEDs would locate. The numbers beside the mixing curves are the galaxy fraction at 1 μm. The magenta arrow shows how reddening affects the E94 radio-quiet mean SED. The numbers under the reddening vector show the $E(B-V)$ values. Left: different regions of the plot correspond to different SED shapes, as shown in the black circles at the four corners. In these four black circles, the SEDs are in the $\log\nu L_\nu$ versus $\log\nu$ plane, with wavelength increasing to the left. The reddening vector here is calculated using SMC reddening law. The points circled in magenta show the position of the outliers in the sample discussed in Paper I (A, B, C, D) and in Section 4.4 of this paper (E, F, G, H). Right: the green square represents mean SED of the 203 *XMM*-COSMOS quasars (Paper I). The green pentagon represents the R06 mean SED ($\alpha_{\rm OPT} = 0.85 \pm 0.03$ and $\alpha_{\rm NIR} = -0.60 \pm 0.05$). The green hexagon represents the Hopkins, Richards & Hernquist (2007) quasar SED template ($\alpha_{\rm OPT} = 0.79 \pm 0.14$ and $\alpha_{\rm NIR} = -0.60 \pm 0.05$). The green triangle represents the Shang et al. (2011) quasar SED template ($\alpha_{\rm OPT} = 0.55 \pm 0.06$ and $\alpha_{\rm NIR} = -0.97 \pm 0.32$). The solid lines in the upper region show 16 different BC03 galaxy models. These 16 models using exponentially declining star formation history with e-folding time-scale τ = (0.01, 0.05, 0.1, 0.3, 0.5, 0.6, 1, 2, 3, 5, 10, 15, 30, 50, 80, 100) Gyr. The blue line is for $\tau = 0.01$ Gyr, while the red line is for $\tau = 100$ Gyr, and the other lines are in cyan. The black tick marks on the lines are for the galaxy model with $\tau = 1$ Gyr with age of the galaxy ($t_{\rm age}$) running from 0.1 Myr to 20 Gyr, in steps of $\log_{10} t_{\rm age} = 0.1$. The magenta arrows in the bottom show tracks for four different reddening curves (Small Magellanic Cloud – 'SMC', Large Magellanic Cloud – 'LMC', Milky Way – 'MW', Calzetti et al. 2000 – 'Calz') applied to E94 radio-quiet mean SED.

quasar–galaxy mixing diagram (hereinafter 'mixing diagram' for short).

With this convenient tool, we can more easily study the evolution of quasar SEDs with physical parameters, identify outliers and estimate host/reddening contributions. This mixing diagram is a generalization of the quasar–galaxy mixing curves in the $(U-B)(B-V)$ colour–colour plane defined for 'N galaxies' by Sandage (1971) and Weedman (1973). The plot is equivalent to a colour–colour plot, but utilizes more photometric bands and is defined in the rest frame. As a result, the mixing diagram can be used for sources at any redshift.

In this paper, we use the mixing diagram to study the SED shape in the OPT to NIR decade (3 μm to 3000 Å) for three type 1 AGN samples: the large *XMM* Cosmic Evolution Survey (*XMM*-COSMOS) type 1 AGN sample (Elvis et al. 2012, Paper I hereinafter), the *Spitzer*-SDSS quasar sample (R06) and the bright quasar sample (E94). Detailed description of the three samples is in Section 3.1. We primarily focus on the *XMM*-COSMOS type 1 AGN sample to demonstrate the major applications of the mixing diagram.

All the wavelengths considered in this paper are in the rest frame. We adopt the *Wilkinson Microwave Anisotropy Probe* 5-year cosmology (Komatsu et al. 2009), with $H_0 = 71\,\mathrm{km\,s^{-1}\,Mpc^{-1}}$, $\Omega_\mathrm{M} = 0.26$ and $\Omega_\Lambda = 0.74$.

2 QUASAR–GALAXY MIXING DIAGRAM

The mixing diagram axes are the 1–3 μm (rest-frame) SED power-law slope (α_NIR) versus the 0.3–1 μm (rest-frame) power-law slope (α_OPT), where $\nu F_\nu \propto \nu^\alpha$. These ranges lie on either side of the 1 μm dip, or inflection point, of the rest-frame SED.

The 1 μm wavelength point is not chosen as the central point arbitrarily. This is where the Wien tail of the blackbody thermal emission of the hottest dust (at the maximum sublimation temperature of ~ 1500 K; Barvainis 1987) begins to outshine the OPT band power law ($\alpha \sim -0.3$) of the SMBH accretion disc (Malkan & Sargent 1982; Sanders et al. 1989; E94; Glikman, Helfand & White 2006).

We tried several different wavelength ranges to calculate the slopes and found that the adopted ranges best represent the dip around 1 μm. If a smaller wavelength range is chosen, the number of photometric points in the range will be greatly reduced, due to the relatively limited photometry coverage (only *JHK* band) in the NIR range. If a longer wavelength range is chosen, a variety of problems would make the estimates of the slope more difficult. For example, shorter wavelengths, into the UV, are more affected by variability and by the Fe II 'small bump' (Wills, Netzer & Wills 1985); longer wavelengths in the NIR encounter a range of cooler dust emission which adds noise to the NIR slope. In the chosen wavelength range, the *XMM*-COSMOS type 1 AGN SED dispersion is invariant in a large range of z and L_bol (Hao et al. 2013a, Paper II hereinafter), which implies an invariant intrinsic dispersion of SED shape in this wavelength range.

To ensure reliable slopes, we require at least three photometric points to define each slope. The robustness of the slope measurement using three or more photometric points was tested in Hao et al. (2011) and found to be good. For the *XMM*-COSMOS quasar sample, the OPT data set is so rich that the mean number of photometry points used in calculating α_OPT is 11.4 ± 6.1, while the infrared data are less rich and the mean number of photometry points used in calculating α_NIR is 4.3 ± 0.7. The errors on the slopes (α_OPT and α_NIR) are the standard errors of the linear fit. The measurement error on the photometry is used in the fitting.

The major characteristics of the mixing diagram are shown in Fig. 1. The E94 radio-quiet (RQ) mean SED template is shown by a red cross. This template is bluer than almost all *XMM*-COSMOS quasars (Paper I), probably due to the $(U-B)$ selection criterion used to select it (Schmidt & Green 1983). The 16 galaxy templates[1] from the 'Spitzer Wide-area Infrared Extragalactic survey (SWIRE) template library' (Polletta et al. 2007) are shown as blue triangles in the left-hand panel of Fig. 1. Lines joining the E94 mean SED to three representative galaxy templates are drawn. These mixing curves are marked at 10 per cent intervals of host galaxy contribution (see Section 2.3 for details).

Note that the slopes are defined in $\log \nu L_\nu$ versus $\log \nu$ plane. Different SED shapes lie in different regions of the mixing diagram, as sketched inside the circles in the four corners of the left-hand panel (wavelength increases to the left in these circles): the *bottom-right* corner shows the 1 μm inflection of an AGN dominated SED; the *upper-left* corner shows the cool starlight peak of a galaxy dominated SED; the *bottom-left* corner shows the rapid drop in the OPT characteristics of a dust reddening dominated SED. The *top-right* corner shows an SED falling throughout the entire OPT–NIR range. This was not a known SED shape until the recent discovery of 'hot dust poor' AGN (hereinafter HDP; Hao et al. 2010, 2011; Jiang et al. 2010), which makes up 10 per cent of the quasar population (Hao et al. 2011).

We will discuss in detail the major characteristics of the mixing diagram as shown in the right panel of Fig. 1 in the following sub-sections.

2.1 Quasar templates

Besides the E94 quasar SED template, there are several recent updates (R06; Hopkins et al. 2007; Shang et al. 2011; Paper I). The comparison of these SED templates was discussed in Paper I.

The R06 SED template was compiled from the *Spitzer*-SDSS sample, containing 259 AGN and used a 'gap repair' technique that replaces the missing photometry with the normalized E94 mean SED to the adjacent available photometry bands. Due to the limited coverage in NIR, the R06 mean SED is therefore, by construction, very similar to the E94 mean SED. Hopkins et al. (2007) simply combined the R06 mean SED with the composite quasar SED (Vanden Berk et al. 2001); thus, it has a shape similar to both R06 and E94. As we can see in the right-hand panel of Fig. 1, the R06 ($\alpha_\mathrm{OPT} = 0.85 \pm 0.03$ and $\alpha_\mathrm{NIR} = -0.60 \pm 0.05$) represented with a pentagon and the Hopkins et al. (2007) template ($\alpha_\mathrm{OPT} = 0.79 \pm 0.14$ and $\alpha_\mathrm{NIR} = -0.60 \pm 0.05$) represented with a hexagon are very close to the E94 template ($\alpha_\mathrm{OPT} = 0.95 \pm 0.04$ and $\alpha_\mathrm{NIR} = -0.72 \pm 0.05$) represented with a cross.

The Shang et al. (2011) mean SED ($\alpha_\mathrm{OPT} = 0.55 \pm 0.06$ and $\alpha_\mathrm{NIR} = -0.97 \pm 0.32$) was calculated using 27 nearby bright RQ quasars. As there is limited coverage in infrared (only three points in the NIR range from the template), there is a large error bar in the NIR slope calculation. The Shang et al. (2011) template is represented with a triangle in the right-hand panel of Fig. 1.

Paper I studied 413 *XMM*-selected COSMOS type 1 AGN. Due to the X-ray selection, there are more quasars in this sample having

[1] The 16 galaxy templates in the 'SWIRE template library' (Polletta et al. 2007) include: 3 elliptical galaxy templates 'Ell2', 'Ell5', 'Ell13' representing elliptical galaxy of age 2, 5 and 13 Gyr, respectively; 7 spiral galaxy templates 'S0', 'Sa', 'Sb', 'Sc', 'Sd', 'Sdm', 'Spi4'; and 6 starburst galaxy templates 'NGC 6090', 'M82', 'Arp 220', 'IRAS 20551−4250', 'IRAS 22491−1808', 'NGC 6240'.

a large host contribution (see also Section 3.2). 203 quasars in the sample can be corrected for host galaxy contribution from the Marconi & Hunt (2003) scaling relationship adding an evolutionary term (Bennert et al. 2010, 2011). The mean host-corrected SED of the 203 *XMM*-COSMOS quasars is represented with a square in the right-hand panel of Fig. 1. We can see that there is still an indication of an excess of host contribution that remains un-corrected. This is likely due to the dispersion in the scaling relationship.

Given the similar location of these templates in the mixing diagram, the results derived from the mixing diagram (e.g. host galaxy fraction, reddening, etc.) would not be significantly affected if R06 or Hopkins et al. (2007) templates are chosen instead of E94. Shang et al. (2011) and Paper I have other contamination factors in the templates themselves that render them not proper to be chosen as the pure quasar template. So we will use E94 template to represent pure quasar SED template for future discussion in this paper.

2.2 Galaxy templates

The 16 SWIRE galaxy SED templates are all from the observations of various types of galaxies (Polletta et al. 2007). Theoretically, models of the galaxy SEDs have been developed based on the stellar population synthesis technique (Bruzual & Charlot 2003, BC03 hereinafter). These models have been successfully used in SED fitting especially in the OPT range (e.g. Ilbert et al. 2009, 2010; Bongiorno et al. 2012). However, these models do not include the dust attenuation and re-radiation, and we are still not sure if all the SEDs produced from these models exist in the real Universe. Here, we plot (Fig. 1, right) the BC03 SED models on the mixing diagram in comparison with the Polletta et al. (2007) observed galaxy templates.

In the right-hand panel of Fig. 1, the galaxy SED model is computed using the preferred Padova 1994 evolutionary tracks (Alongi et al. 1993; Bressan et al. 1993; Fagotto et al. 1994a,b; Girardi et al. 1996) assuming a universal initial mass function from Chabrier (2003) and an exponentially declining star formation history. The star formation rate $\psi(t)$ is expressed as $\psi(t) = 1\,\mathrm{M}_{\odot}\tau^{-1}\exp(-t/\tau)$, where τ is the e-folding time-scale. We show models for 16 different e-folding time-scales τ = (0.01, 0.05, 0.1, 0.3, 0.5, 0.6, 1, 2, 3, 5, 10, 15, 30, 50, 80, 100) Gyr, ranging a variety of star formation history.

The lines shown are for galaxies with ages ($t_{\rm age}$) running from 0.1 Myr to 20 Gyr for each e-folding time-scale model. The black tick points on the lines are for a galaxy model with $\tau = 1$ Gyr in steps of $\log_{10}t_{\rm age} = 0.1$. For different e-folding time-scales, the young galaxies ($t_{\rm age} < 0.01$ Gyr) are quite similar to each other. However, for older galaxies ($t_{\rm age} > 0.1$ Gyr), the positions in this plot are quite different for different e-folding time-scales. For example, for $\tau = 0.01$ Gyr model (blue solid line), the oldest galaxy ($t_{\rm age} = 20$ Gyr) reaches the leftmost region of the diagram and for $\tau = 100$ Gyr model (red solid line), the oldest galaxy ($t_{\rm age} = 20$ Gyr) only reaches the Spi4 position. All the galaxies in the $\tau = 100$ Gyr model fail to overlap with the observed Polletta et al. (2007) galaxy region. When we increase the e-folding time-scale, the position of the galaxies with the same age at $t_{\rm age} > 0.1$ Gyr move from the left to the right on the diagram. The distances among the lines on the mixing diagram with different e-folding time-scales lie within the error bar of the slopes except for the $\tau = 0.01$ Gyr model, which show a wave at $0.01\mathrm{Gyr} < \mathrm{t}_{\rm age} < 1\,\mathrm{Gyr}$. This wave also exists in other lines with smaller size and at $1 < \alpha_{\rm OPT} < 1.5$. The wave may have caused by the molecular feature in the atmosphere of cool/old stars.

From $t_{\rm age} > 0.1$ Gyr, the $\alpha_{\rm NIR}$ values are almost constant compared to the huge change in $\alpha_{\rm OPT}$. This is reasonable because the NIR SED mainly comes from the emission of old stars whereas the OPT SED mainly comes from the emission of young stars. As an exponentially declining star formation history is assumed, when the galaxy gets old enough, the star formation rate is low, which means that the young star population becomes very small. So the OPT SED changes a lot, but the NIR SED almost stays constant.

Compared to SWIRE galaxy templates, the BC03 models show very blue galaxies located on the upper-right corner of the mixing diagram and show less spread in the $\alpha_{\rm NIR}$ direction. The blue galaxies are typically very young and they would be expected to contain large amount of gas. These galaxies are very rare in the redshift range of current major surveys and tend to be more common for high reshifts ($z > 6$; Bouwens et al. 2012). These very blue galaxies are so extremely short-lived that they are expected to be a very small fraction in any sample of galaxies. For example, in Ilbert et al. (2010), SED fitting analysis is performed to ∼200 000 Infrared Array Camera (IRAC)-selected galaxies with $0.2 < z < 2$ in the COSMOS field. They find that only a few per cent have $t_{\rm age} < 0.5$ Gyr and most of them are fitted with a significant extinction.

One would suspect that the presence of a young population on top of an older population could mimic a blue non-thermal quasar-like OPT spectrum. However, in practice, the chance is low, because, to reach the slope, the star formation rate of the young population would be too extreme. Also, if this were commonly true, optically selected type 1 AGN would be severely diluted by starbursts, which is not seen.

The possible presence of very young galaxy models also provides an alternative explanation to the HDP AGN SED that is the normal quasar SED with a large fraction of young host galaxy. But this explanation would require the quasar to be active simultaneously with a strong starburst, which is not seen in large samples (e.g. Kewley et al. 2006; Schawinski et al. 2009; Wild et al. 2010).

In this paper, to be consistent with the quasar template we use (E94, which has been derived from observed SEDs), we only use the observed Polletta et al. (2007) SWIRE galaxy templates for further discussion.

2.3 Galaxy fraction mixing curves

We can quantify the host galaxy contribution fraction $f_{\rm g}$ at 1 μm for any quasar, assuming that the E94 RQ template represents a pure AGN SED. A definition similar to $f_{\rm g}$ is widely used in SED fitting with different normalization wavelengths (e.g. Salvato et al. 2009, Merloni et al. 2010). The parameter $f_{\rm g}$ is defined as the galaxy fraction at 1 μm, and it describes how close the observed SED is to the galaxy templates. First, we normalize both the galaxy and AGN template at 1 μm. Then, the mixture of some fraction of galaxy ($f_{\rm g}$) and some fraction of AGN (1-$f_{\rm g}$) emission can be calculated accordingly. Suppose that at frequency ν the galaxy template SED luminosity is νL_{ν}^{G} and the AGN template (E94) SED luminosity is νL_{ν}^{A}, then the mixing of the two SEDs luminosity is

$$\nu L_{\nu}^{\rm mix} = f_{\rm g}\nu L_{\nu}^{G} + (1 - f_{\rm g})\nu L_{\nu}^{A}.$$

The black curves in Fig. 1 show the slopes of SED templates obtained by mixing the AGN and galaxy templates with values of $f_{\rm g} = 0 - 1$. The mixing curves of the starburst galaxy 'NGC 6090' and the spiral galaxy 'Spi4' define the red and blue boundaries of the possible slopes obtained by mixing the E94 SED with all 16 galaxy templates in the SWIRE library. The spectral slopes for mixtures of E94 with Spi4, Ell5, Sb, S0 and NGC 6090 for 11 values of $f_{\rm g}$

Table 1. Spectral slopes for different f_g values (mixing curve) assuming E94 mean SED as the pure quasar SED.[a]

f_g	Spi4		Ell5		Sb		S0		NGC 6090	
	α_{OPT}	α_{NIR}	α_{OPT}	α_{NIR}	α_{OPT}	α_{NIR}	α_{OPT}	α_{NIR}	α_{OPT}	α_{NIR}
0.0	0.950	−0.719	0.950	−0.719	0.950	−0.719	0.950	−0.719	0.950	−0.719
0.1	0.876	−0.621	0.857	−0.618	0.862	−0.617	0.860	−0.617	0.864	−0.620
0.2	0.794	−0.513	0.752	−0.506	0.762	−0.506	0.759	−0.506	0.766	−0.511
0.3	0.702	−0.394	0.634	−0.382	0.648	−0.383	0.641	−0.383	0.655	−0.392
0.4	0.598	−0.262	0.496	−0.244	0.515	−0.246	0.505	−0.245	0.525	−0.260
0.5	0.480	−0.112	0.334	−0.086	0.357	−0.090	0.341	−0.089	0.372	−0.111
0.6	0.342	0.060	0.138	0.097	0.164	0.089	0.140	0.091	0.184	0.059
0.7	0.178	0.263	−0.109	0.316	−0.082	0.302	−0.119	0.304	−0.053	0.257
0.8	−0.024	0.509	−0.439	0.586	−0.415	0.563	−0.475	0.566	−0.373	0.497
0.9	−0.286	0.823	−0.934	0.941	−0.925	0.902	−1.037	0.906	−0.857	0.800
1.0	−0.656	1.264	−1.972	1.469	−2.044	1.396	−2.447	1.403	−1.876	1.218

[a]A portion of the table is shown here for guidance. The complete table for 16 SWIRE galaxy templates will be available online.

are listed in Table 1. The complete table for all the 16 templates is available online.

2.4 Reddening vectors

Intrinsic reddening in AGN is often important in defining their SEDs (e.g. Ward et al. 1987; O'Brien, Wilson & Gondhalekar 1988; Young, Elvis & Risaliti 2008; Shang et al. 2011). The magenta arrows in Fig. 1 show α_{OPT} and α_{NIR} for the E94 SED when reddened by $E(B-V) = 0 - 1$ mag.

We consider four different reddening laws: Small Magellanic Cloud (SMC), Large Magellanic Cloud (LMC), Milky Way (MW) and Calzetti et al. (2000, hereinafter Calz). For the SMC, LMC and MW reddening laws, the reddening of the E94 SED is derived with the IDL de-reddening routines '`FM_UNRED.PRO`' (for SMC and LMC) and '`CCM_UNRED.PRO`' (for MW), which all use the Fitzpatrick (1999) parametrizations of the SMC (Gordon et al. 2003), LMC (Misselt, Clayton & Gordon 1999) and the MW (Cardelli, Clayton & Mathis 1989; O'Donnell 1994) extinction curves. For the Calz reddening law, the reddening is derived with IDL de-reddening routine '`CALZ_UNRED.PRO`', which uses the Calz recipe developed for galaxies where massive stars dominate the radiation output. The SMC reddening law (Gordon et al. 2003) is typically used for quasars, and is shown to fit reddening in quasars more effectively than an LMC or MW reddening law (Hopkins et al. 2004; Richards et al. 2003). Reddening primarily affects α_{OPT}. The effect of reddening is reported in Table 2.

Using the reddening vector, we can estimate f_g and $E(B-V)$ from the mixing diagram for sources lying off the E94-host mixing curves towards the lower left. For each source, we can draw a line parallel to the reddening curve (black dashed line in Fig. 1). The crossing point of this line and the mixing curve shows approximately the value of f_g. The length of the parallel line gives an estimate of $E(B-V)$. We use this technique in Sections 4.2 and 4.3.

Different reddening laws could cause different f_g and $E(B-V)$ derived from the mixing diagram. As we can see from the right-hand panel of Fig. 1, the SMC, LMC and MW reddening vectors are closely similar to each other. The Calz reddening vector is significantly different from the other three reddening laws. This reddening law is generally used for star-forming galaxies (Calz) not AGN. Gordon et al. (2003) performed a comparison between SMC, LMC and MW reddening laws and found that the extinction curves only begin to diverge shortwards of ∼2000 Å and at rest-frame near-UV (∼2500 Å) through NIR (∼1 μm); the three laws are extremely similar. So for the rest-frame wavelength range in which the mixing diagram is defined (3000 Å to 1 μm and 1–3 μm), the results will not be significantly different if we choose either SMC, LMC or MW reddening law. We will only consider the SMC reddening law in the following discussion.

Table 2. Reddening Vector for E94.

Ext. law	SMC		LMC		MW		Calz	
$E(B-V)$	α_{OPT}	α_{NIR}	α_{OPT}	α_{NIR}	α_{OPT}	α_{NIR}	α_{OPT}	α_{NIR}
0.0	0.950	−0.719	0.950	−0.719	0.950	−0.719	0.950	−0.719
0.1	0.596	−0.798	0.596	−0.798	0.604	−0.807	0.553	−0.890
0.2	0.242	−0.877	0.242	−0.877	0.257	−0.895	0.156	−1.060
0.3	−0.112	−0.956	−0.112	−0.956	−0.089	−0.982	−0.241	−1.231
0.4	−0.465	−1.034	−0.465	−1.034	−0.435	−1.070	−0.639	−1.402
0.5	−0.819	−1.113	−0.819	−1.113	−0.781	−1.158	−1.036	−1.572
0.6	−1.173	−1.192	−1.173	−1.192	−1.128	−1.246	−1.433	−1.743
0.7	−1.527	−1.271	−1.527	−1.271	−1.474	−1.333	−1.830	−1.914
0.8	−1.881	−1.350	−1.881	−1.350	−1.820	−1.421	−2.227	−2.084
0.9	−2.235	−1.428	−2.235	−1.428	−2.166	−1.509	−2.624	−2.255
1.0	−2.588	−1.507	−2.588	−1.507	−2.513	−1.597	−3.021	−2.426

3 MIXING DIAGRAM FOR TYPE 1 AGN SAMPLES

3.1 Type 1 AGN samples

The three type 1 AGN samples we used in this paper are:

(1) The *XMM*-COSMOS type 1 AGN Sample (XC413; Paper I). The COSMOS field (Scoville et al. 2007) was imaged in X-rays with *XMM-Newton* for a total of ∼1.5 Ms (Cappelluti et al. 2007, 2009; Hasinger et al. 2007). OPT identifications were made by Brusa et al. (2007, 2010) for the entire *XMM*-COSMOS sample, who gave photometric properties and redshifts for each X-ray point source. From this complete sample, we extracted a sample of 413 type 1 AGN, defined by having broad line FWHM > 2000 km s^{-1}. The XC413 catalogue was described in detail in Paper I.

This sample has full wavelength coverage from radio to X-ray (for a total of 43 photometric bands, Paper I) and high confidence level spectroscopic redshifts (Lilly et al. 2007, 2009; Schneider et al. 2007; Trump et al. 2009). In this paper, we also add the recently released *H*-band photometry from Canada France Hawaii Telescope/Wide-field Infrared Camera (CFHT/WIRCam) (McCracken et al. 2010). Now 405 out of the 413 *XMM*-COSMOS quasars have *H*-band photometry, compared to 252 out of 413 in Paper I. As described in Paper I, the photometric data obtained from different telescopes and with different seeing were matched and the aperture fluxes were all transformed to total flux according to the point spread function simulation for each telescope (e.g. Brusa et al. 2007; Capak et al. 2007). As in Paper I, in order to reduce the extra error in the SED slope measurement that can be caused by variability of quasars, we used only the OPT photometric data obtained in a shorter time period (2004–2008) close to the time of the infrared *Spitzer*-IRAC data. The COSMOS type 1 AGN sample has an extremely rich coverage (36 bands) in the OPT–NIR range. The objects have redshifts $0.1 \leq z \leq 4.3$ and magnitudes $16.9 \leq i_{\rm AB} \leq 24.8$, with 94–98 per cent being RQ (Hao et al. 2013b).

In this sample, 206 quasars have published black hole mass measurements (Trump et al. 2009b; Merloni et al. 2010), which are based on the scaling relationship between broad emission line (BEL) full width at half-maximum (FWHM) and black hole mass (Vestergaard 2004). For the quasars with only zCOSMOS spectrum, the black hole mass was estimated for only those with Mg II lines in the spectrum (Merloni et al. 2010), using the calibration of McLure & Jarvis (2002). For the rest of the sample, the BELs are located close to the ends of the spectra, so reliable black hole mass estimates cannot be made. We call the sub-sample with black hole mass estimates SS206 ('SS' stands for sub-sample) hereinafter.

(2) The *Spitzer*-SDSS Sample (R06). The R06 sample consists of 259 *Spitzer* sources identified with Sloan Digital Sky Survey (SDSS) quasars in four different degree-scale fields, and is, therefore, mid-IR identified and optically selected. The redshift range covered is $z = 0.14$–5.2 with 93 per cent being at $z < 3$. Most (215/259) of the R06 sources did not have 2MASS *JHK* photometry. Details about how we measured the slopes with this sample were described in Hao et al. (2011).

(3) The bright quasar sample (E94). This sample consists of 42 quasars in the redshift range $z = 0.025$–0.94, with 80 per cent of them being at $z < 0.3$. The OPT photometry was obtained at the FLWO (F. L. Whipple Observatory) 24 inch telescope within one week of the Multiple Mirror Telescope (MMT) FOGS (Faint Object Grism Spectrograph) spectroscopic observations. The NIR data were obtained with MMT and IRTF. More details on the observation can be found in E94. The E94 SEDs have been corrected for host galaxy contamination by subtracting the host galaxy template SED based on the Sbc galaxy model of Coleman, Wu & Weedman (1980). The E94 sample has bolometric luminosities ($\log L_{\rm bol}$) in the range of 44.6–47.2 erg s^{-1} with mean of 45.75 erg s^{-1}. We recalculated the E94 bolometric luminosities with the same cosmological parameters used for XC413. Compared to XC413, E94 sample is on average more luminous and contains less low-luminosity quasars than the XC413. The Eddington ratio of the Palomar-Green (PG) quasars (including E94 sample) is comparable to that of the XC413 (Sikora, Stawarz & Lasota 2007; Paper II).

3.2 Mixing diagram for the quasar samples

We plot the XC413 sample on the mixing diagram in Fig. 2. The distribution is continuous and largely lies between the E94 mean SED and the galaxy templates, along the mixing curves, with some spread in the reddening direction to values as large as $E(B-V) \sim 0.6$, but mostly with $E(B-V) < 0.3$. The green crosses represent objects with black hole mass estimates (Paper II), which span the range of the entire sample in the mixing diagram.

The diagram shows that about 90 per cent of the sources lie in the left-hand triangular 'mixing wedge' between the mixing curves and the reddening vector. The SEDs of these AGN can be accounted for with a simple combination of an E94 quasar SED, plus a galaxy contribution and reddening. This suggests that the AGN sample is consistent with a single intrinsic SED shape, closely resembling the E94 mean quasar SED (see also in Section 4.1, where we compare in detail the XC413 and the E94 quasar sample).

There are several sources outside the wedge, which are outliers with respect to the bulk of the type 1 AGN population (see Section 4.4 for details). As the galaxy SED dispersion is expected to be broader than the 16 Polletta templates, it is not surprising to see three sources (XID = 4, 1559, 5617) beyond the SWIRE galaxy template

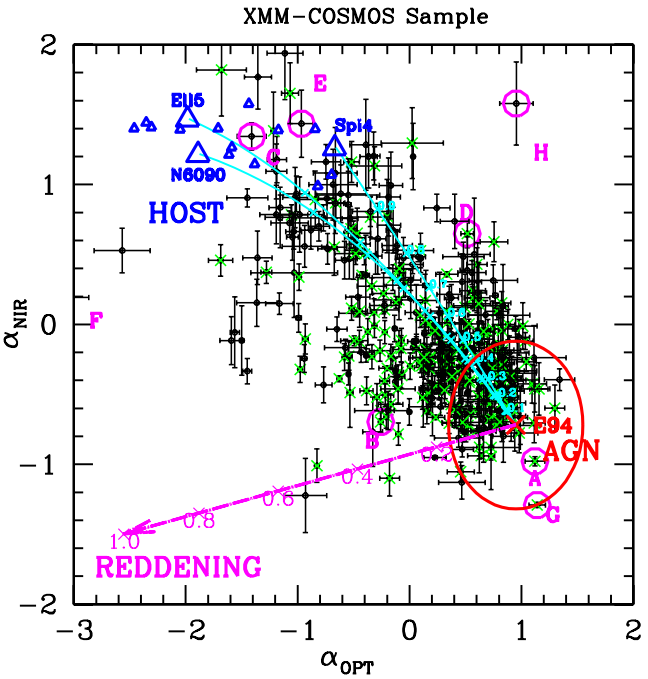

Figure 2. The mixing diagram of the *XMM*-COSMOS type 1 AGN sample (XC413). The other points and lines are colour-coded as in Fig. 1. The green crosses show the 206 quasars with black hole mass estimates (the SS206 sub-sample; Paper II).

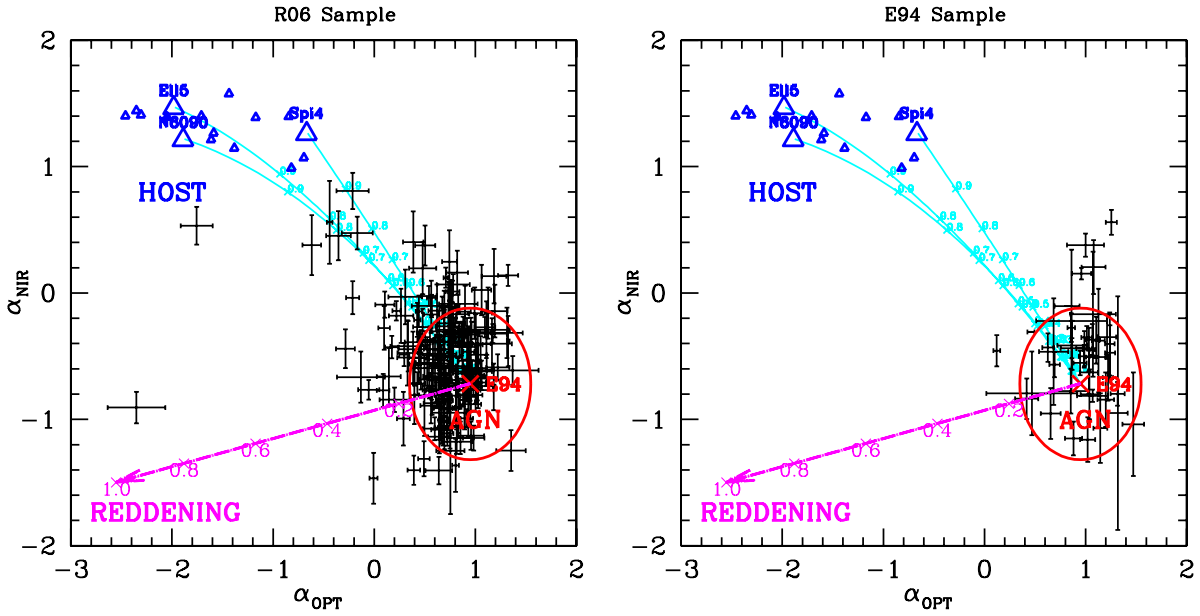

Figure 3. The mixing diagram of the *Spitzer*-SDSS quasar sample (R06, left) and the bright quasar sample (E94, right). The other points and lines are colour-coded as in Fig. 2.

region (still within 1σ) that would formally require $f_g > 1$. We excluded these sources when using the mixing diagram to calculate f_g (see Section 4.2 for details).

We also plot the mixing diagram for the *Spitzer*-SDSS quasar sample (R06) and the bright quasar sample (E94), shown in Fig. 3 (see also Hao et al. 2011). For the optically selected R06 sample, quasars by selection are more clustered in the quasar-dominated region unlike the X-ray-selected XC413, which includes more sources with low quasar to host galaxy contrast. The E94 quasars have been corrected for host galaxy contribution. Thus they are, by construction, clustered around the E94 mean (red cross) in the quasar-dominated region. Compared to the E94 sample, the R06 sample is not as blue in the OPT.

3.3 Intrinsic slope dispersion

We selected an SS of AGN-dominated XC413 SEDs with $\alpha_{OPT} > 0.2$ in order to exclude galaxy- or reddening-dominated sources. This sample has a mean slope $\bar{\alpha}_{OPT} = 0.63$ (standard deviation $\sigma_{OPT} = 0.24$), and $\bar{\alpha}_{NIR} = -0.31$ (standard deviation $\sigma_{NIR} = 0.36$). The E94 RQ mean [α_{OPT}(E94) = 0.95, α_{NIR}(E94) = −0.72, see values in Table 1 for $f_g = 0$] lies at the extreme blue end of the distribution.

To estimate the intrinsic dispersion within the AGN-dominated XC413 SS, we removed the effect of measurement error, namely $\sigma_{INT} = \sqrt{\sigma^2 - Err^2}$. The mean of the measurement error for α_{OPT} is $Err_{OPT} = 0.09$, and for α_{NIR} is $Err_{NIR} = 0.12$. The intrinsic dispersion thus is $\sigma_{INT,\,OPT} = 0.22$ and $\sigma_{INT,\,NIR} = 0.34$, respectively. Therefore, the intrinsic dispersion of the SED shape is two to three times the measurement error and seems to be significant.

The equivalent intrinsic dispersions in the E94 and R06 sample were estimated by Hao et al. (2011), who found: $\sigma_{E94,\,INT,\,OPT} = 0.25$, $\sigma_{E94,\,INT,\,NIR} = 0.32$, $\sigma_{R06,\,INT,\,OPT} = 0.23$ and $\sigma_{R06,\,INT,\,NIR} = 0.36$, respectively. The intrinsic dispersions are thus similar for all the three samples.

To compare the intrinsic dispersion of these three samples more rigorously, we applied the Bayesian method of Kelly (2007). This assumes that the intrinsic distribution of the slopes is a mixture of Gaussians. The probability distributions of the differences in slope dispersion between the samples are shown in Fig. 4. For the dispersion in α_{OPT}, the significance of the difference between the *XMM*-COSMOS and R06 sample is 0.16σ; between *XMM*-COSMOS and E94 sample is 0.11σ and between R06 and E94 sample is 0.08σ. Therefore, the intrinsic dispersions of the α_{OPT} are consistent with being the same for all the three samples. For α_{NIR}, the significance of the difference between the *XMM*-COSMOS and R06 sample is 0.02σ; between the *XMM*-COSMOS and E94 sample is 0.08σ and between the R06 and E94 sample is 0.06σ. As in the simpler analysis, the intrinsic dispersions of the α_{OPT} and α_{NIR} are consistent with being the same for all the three samples.

Using this result we can create a more rigorous AGN-dominated sample using the intrinsic dispersion to define a radius in the (α_{OPT}, α_{NIR}) plane within which such AGN must lie. As the distribution of the quasars is continuous, different radii define different populations of quasars. We define a circle centred on the E94 RQ mean SED template with a radius of 0.6 on the mixing diagram to define AGN-dominated sources. This is approximately $3\sigma_{OPT}$ and $1.5\sigma_{NIR}$ of the intrinsic dispersion. Note that the AGN-dominated circle chosen here is somewhat arbitrary and is used just for illustration. Different radii or even shapes of the AGN-dominated region can be chosen for different purposes. For the XC413 sample, the sources within the dispersion circle populate mainly the upper-left quadrant, similar to the R06 sample, but unlike the host-corrected E94 sample. We will discuss this more in Section 4.1.

4 APPLICATION OF THE MIXING DIAGRAM TO THE XC413 SAMPLE

4.1 SED evolution on the mixing diagram

Paper II studied the evolution of the mean and dispersion of the SED with physical parameters (redshift z, bolometric luminosity

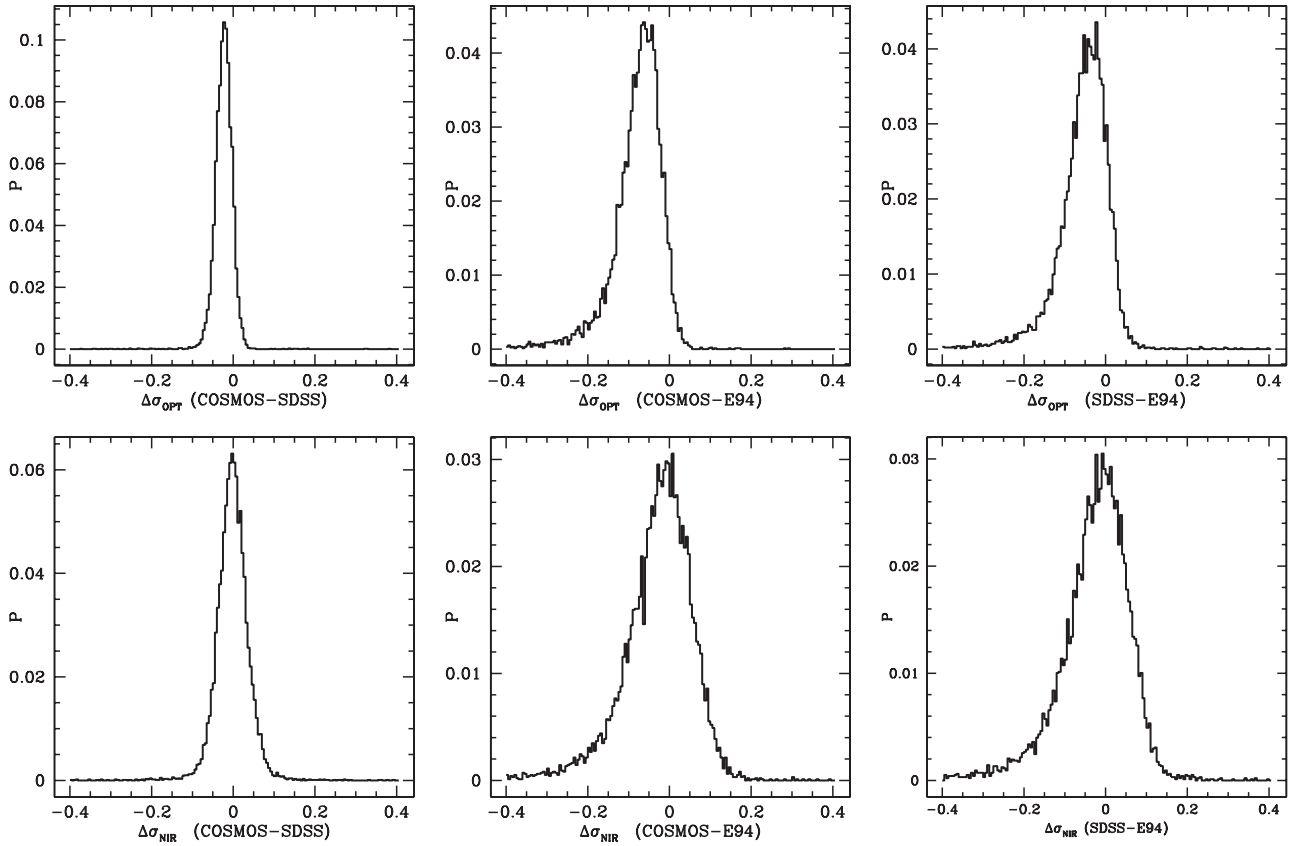

Figure 4. The probability distribution of the difference in slope dispersion in the three samples.

$L_{\rm bol}$, black hole mass $M_{\rm BH}$ and Eddington ratio $\lambda_{\rm E}$[2]) for the 407 RQ quasar in the XC413 sample. Paper II showed that there is no obvious evidence for evolution of the quasar SED shape with respect to these parameters. The study was limited by the difficulties of host galaxy subtraction. The conclusions are fully based on the assumption that host galaxy correction according to the black hole mass and bulge mass scaling relationship adding an evolutionary term is reliable. The mixing diagram is a new tool to address this issue, with no need to rely on the assumption that the host correction is properly done. That is because the diagram itself can clearly show the contribution from the host galaxy.

In order to search for quasar SED evolution with respect to physical parameters, we plotted the mixing diagram for the XC413 sample in bins of z, $\log L_{\rm bol}$, and for the SS206 sample with two additional parameters $\log M_{\rm BH}$ and $\log \lambda_{\rm E}$, because the black hole mass estimates are only available for these 206 quasars in XC413 (see Section 3.1). We divided the sample in four bins: in z [0 – 1 – 2 – 3 – 4.3], in $\log L_{\rm bol}$ [44.2 – 45.2 – 45.8 – 46.4 – 47.3], in $\log(M_{\rm BH}/{\rm M}_\odot)$ [7.1 – 7.7 – 8.3 – 8.9 – 9.4], and in $\log \lambda_{\rm E}$ [(−1.9) – (−1.2) – (−0.6) – 0 – 0.7], respectively. For each physical parameter the four bins have approximately equal bin size, so it is easy to compare bins. The resulting mixing diagrams are shown in Figs 5 and 6.

To look for any SED evolution in smaller steps, we colour coded the quasars in each bin for four equal sub-bins (Figs 5 and 6). In each z and $\log L_{\rm bol}$ mixing diagram, the black, red, green and blue points represent quasars with small to large z and $\log L_{\rm bol}$, with the sub-bin size of 0.25. Similarly, in each $\log M_{\rm BH}$ and $\log \lambda_{\rm E}$ mixing diagram, the black, red, green and blue colours represent small to large values, with sub-bin size of 0.15.

For the lowest bin of each parameter ($0 < z < 1$, $44.2 < \log L_{\rm bol} < 45.2$, $7.1 < \log(M_{\rm BH}/{\rm M}_\odot) < 7.7$, $-1.9 < \log \lambda_{\rm E} < -1.2$), almost all of the sources lie within the mixing wedge defined by the AGN–host mixing curve, allowing for the 1σ range of the E94 mean SED slope, mixing curve and the reddening curve.

For high values of each parameter, the quasars (Figs 5 and 6) cluster close to the quasar-dominated region (within the red circle), while in the lower value bins the quasars spread out along the mixing curves towards the galaxy template locations. This effect is the strongest in $\log L_{\rm bol}$ bins. For different $\log L_{\rm bol}$ bins, the cluster of quasar locations clearly drifts along the mixing curves, from completely outside the AGN-dominated circle at low $\log L_{\rm bol}$, with many sources lying near the pure galaxy-dominated region, to almost completely inside the dispersion circle at high $\log L_{\rm bol}$. This is expected, as the galaxy luminosity is generally no more than 10^{45} erg s^{-1} (Cirasuolo et al. 2007). Thus for extremely high-luminosity sources, the AGN outshines the galaxy, especially in the OPT. However, the M–σ relation puts a limit on how much a quasar can outshine its host galaxy (Paper I, II).

Although almost all of the highest luminosity quasars (Fig. 5) lie within the AGN-dominated circle, they are not centred at the E94 RQ mean. Instead, they lie overwhelmingly in the upper-left quadrant of the dispersion circle, similar to the R06 sample as shown in the left-hand panel of Fig. 3. This suggests that some shift with respect to the E94 SED is present in both spectral slopes. For these

[2] $\lambda_{\rm E} = \frac{L_{\rm bol}}{L_{\rm Edd}} = \frac{L_{\rm bol}}{\frac{4\pi G c m_p}{\sigma_e} M_{\rm BH}} = \frac{L_{\rm bol}}{1.26 \times 10^{38} (M_{\rm BH}/{\rm M}_\odot)}$

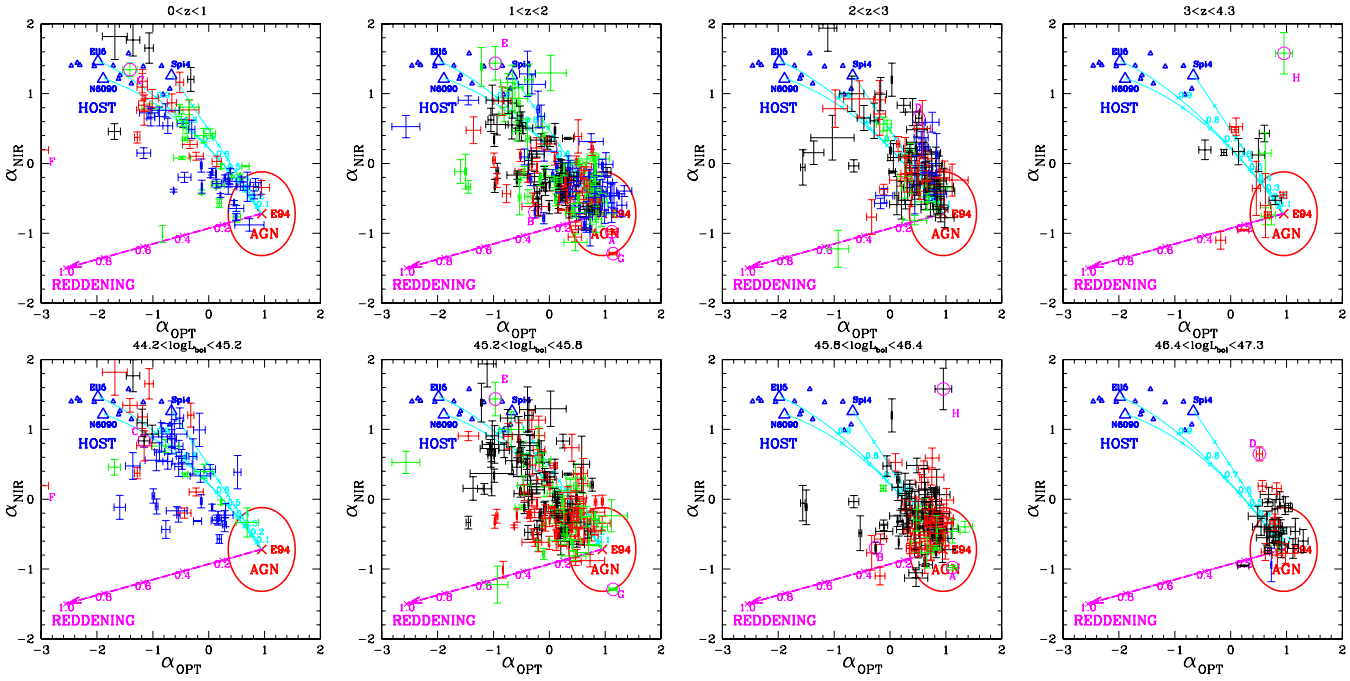

Figure 5. $\alpha_{\rm NIR}$ versus $\alpha_{\rm OPT}$ plot for the XC413 sample in z bins [0 – 1 – 2 – 3 – 4.3] (top row) and log$L_{\rm bol}$ bins [44.2 – 45.2 – 45.8 – 46.4 – 47.3] (bottom row). Different colours of the points in each plot represent quasars in different sub-bins, with bin width 0.25, from low to high: black, red, green and blue. The E94 mean SED is shown as the red cross, with the galaxy templates from the SWIRE (Polletta et al. 2007, blue triangles). The cyan lines are the quasar–host mixing curves. The purple line represents the reddening vector. The red circle shows the dispersion circle.

highest luminosity quasars, the mean $\alpha_{\rm OPT}$ is 0.78, versus 0.95 for E94 mean SED, with $\sigma = 0.21$; and the mean $\alpha_{\rm NIR}$ is -0.44, versus -0.72 for E94 mean SED, with $\sigma = 0.30$. In XC413, the slopes of the highest luminosity quasars are shifted by $\sim 1\sigma$ relative to the E94 RQ mean SED. This may be an intrinsic shift, or may indicate a non-negligible host galaxy component even in these luminous quasars.

To compare in detail the highest luminosity quasars in XC413 and E94, we checked the eight E94 quasars which lie in the same highest luminosity range (above 2×10^{46} erg s^{-1}). The mean $\alpha_{\rm OPT,\,E94}$ of these eight high-luminosity E94 quasars is 0.93 with $\sigma = 0.26$, almost exactly the same as the OPT slope of E94 mean SED, and bluer ($\sim 1\sigma$) than the XC413 high-luminosity quasars. Instead, the mean $\alpha_{\rm NIR,\,E94}$ of these eight E94 quasars is -0.19, with $\sigma = 0.38$, which is much flatter than the NIR slope of E94 mean SED, and even flatter than the XC413 high-luminosity quasars. This difference is mainly due to the two HDP quasars in these eight E94 quasars (Hao et al. 2011). From this comparison, we can only conclude that the highest luminosity E94 quasars are bluer than the highest luminosity XC413 quasars. We are not sure if this result can be explained by selection effects only.

In the higher z bins, a population of outliers is present towards the top-right corner. These outliers are the HDP quasars discussed in detail in Hao et al. (2010, 2011). The fraction of sources outside the mixing wedge is quite similar in the top three log $L_{\rm bol}$, log $M_{\rm BH}$ and log $\lambda_{\rm E}$ bins. This result agrees with the lack of evolution in HDP fraction with $M_{\rm BH}$ and $\lambda_{\rm E}$ (Hao et al. 2010, 2011).

In first approximation, the contrast between nuclear AGN continuum and host galaxy in the B band (rest frame) can be expressed in a single formula (Merloni & Heinz 2012):

$$\frac{L_{\rm AGN,B}}{L_{\rm host,B}} = \frac{\lambda_{\rm E}}{0.1}\frac{(M_*/L_B)_{\rm host}}{3(\rm M_\odot/L_\odot)}(B/T),$$

where $(M_*/L_B)_{\rm host}$ is the mass-to-light ratio of the host galaxy and (B/T) is the bulge-to-total galactic stellar mass ratio. So for typical mass-to-light ratios and bulge-to-total galactic stellar mass ratios, the contrast will be smaller if $\lambda_{\rm E}$ is smaller, as shown in the bottom row of Fig. 6, from left to right. When $\lambda_{\rm E}$ is getting larger, the quasars generally drift towards the quasar dominated direction (smaller $f_{\rm g}$).

A minority of XC413 quasars in each of the lower bins of z, log $L_{\rm bol}$ lie in the highly reddened region [$E(B-V) > 0.4$, Fig. 5]. For example, for the lowest z bin, the fraction is 6 per cent (4 out of the 71 sources). In SS206 (Fig. 6), quasars in the highly reddened region only exist in the lower bins of z and log $L_{\rm bol}$. This effect is not so evident in log $M_{\rm BH}$ and log $\lambda_{\rm E}$, where a small fraction of highly reddened quasars appear in high log $M_{\rm BH}$ or log $\lambda_{\rm E}$ bins. Extremely low Eddington ratio AGN ($\lambda_{\rm E} < 10^{-4}$) tend to have red OPT SED, unlike the typical quasars ($\lambda_{\rm E} > 0.01$) with 'big-blue-bump' (Ho 2008; Trump et al. 2011). In SS206, we do not see any obvious trend that small Eddington ratio quasars are more reddened for the typical quasars. This is probably due to the small Eddington ratio range in SS206 compared to the large difference between the low-luminosity AGN and the normal AGN.

4.2 Inferred host galaxy fraction

The mixing diagram provides a new estimate of the galaxy fraction $f_{\rm g}$ (Section 2.4). The errors on the $f_{\rm g}$ estimates are caused by the error on the slopes, due to linear fitting of the SEDs. Different galaxy templates also give slightly different $f_{\rm g}$ values. Fig. 7 compares the values for two templates. The differences are negligible and almost unbiased, compared to the errors on $f_{\rm g}$. The correlation coefficient is 1 (precise to the fourth place after decimal). If we fit a straight line, the best-fitting slope is 1.06 ± 0.001, very close to 1.

We can compare $f_{\rm g}$ with host galaxy fractions derived with three other methods: using bulge–black hole scaling relations, direct

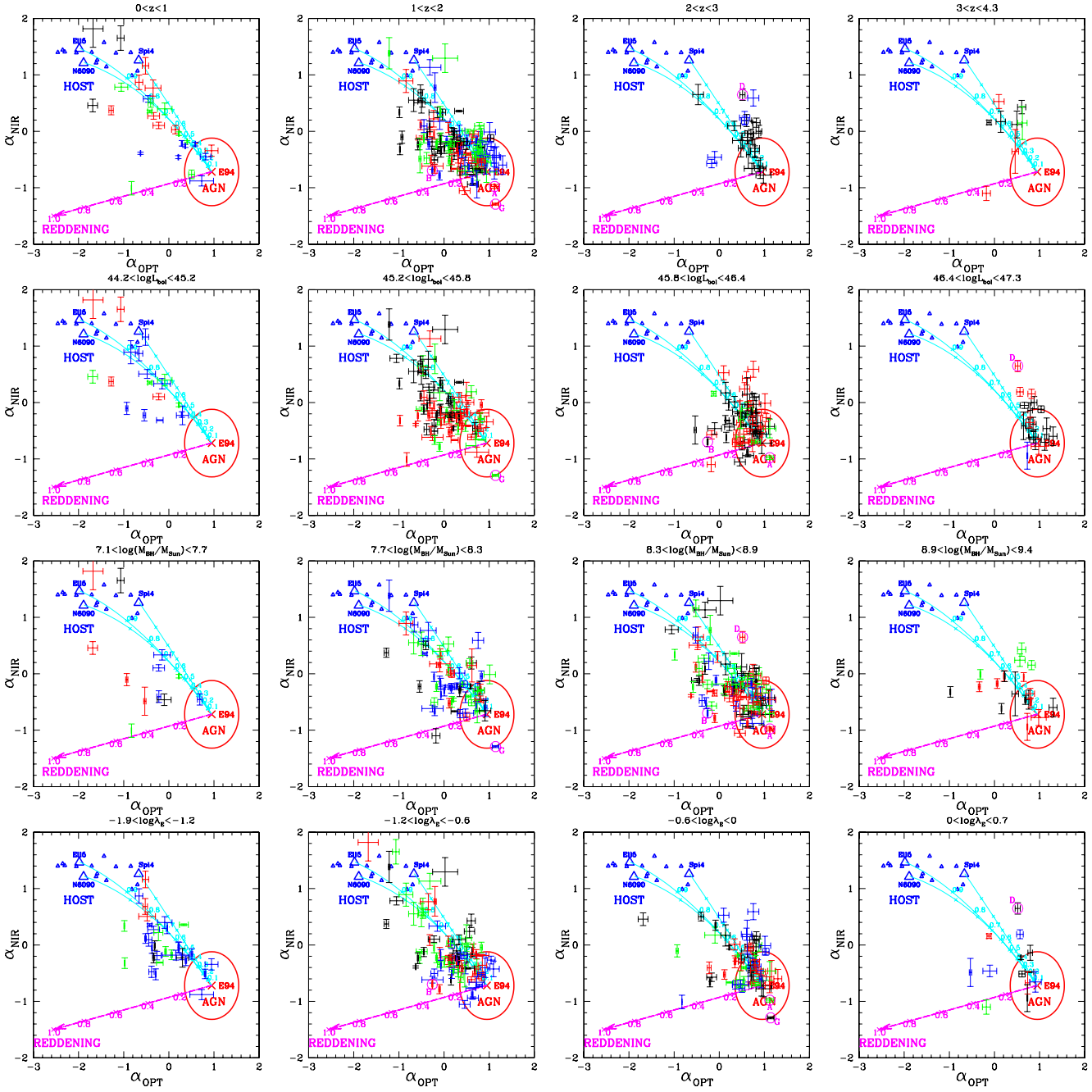

Figure 6. $\alpha_{\rm NIR}$ versus $\alpha_{\rm OPT}$ plot for SS206 sample in z bins [0 – 1 – 2 – 3 – 4.3] (top row), $\log L_{\rm bol}$ bins [44.2 – 45.2 – 45.8 – 46.4 – 47.3] (second row), $\log(M_{\rm BH}/{\rm M}_{\odot})$ bins [7.1 – 7.7 – 8.3 – 8.9 – 9.4] (third row) and $\log\lambda_{\rm E}$ bins [(−1.9) – (−1.2) – (−0.6) – 0 – 0.7]. Different colour of points in each plot represent quasars in different sub-bins, with sub-bin width 0.25 for z and $\log L_{\rm bol}$ bins and sub-bin width 0.15 for $\log M_{\rm BH}$ and $\log\lambda_{\rm E}$ bins, from low to high: black, red, green and blue. The plots are colour-coded as in Fig. 5.

imaging and SED fitting. The three methods are briefly described below.

(1) *Black hole mass–galaxy bulge scaling relations*. For the 203 quasars in SS206, following Paper I, we used the relationship between the black hole mass and NIR bulge luminosity (table 2 of Marconi & Hunt, 2003) adding an evolutionary term (Bennert et al. 2010, 2011) to estimate the host galaxy contribution:

$$\log(L_{J,{\rm Gal}}) = 0.877\log(L_{\rm bol}) + 3.545 - 0.877\log\lambda_{\rm E} - 1.23\log(1+z). \quad (1)$$

We used the Ell5 galaxy template to calculate the rest-frame 1 μm host luminosity. In this band, the differences among different galaxy templates are small. With the host luminosity we can calculate the galaxy fraction at rest-frame 1 μm ($f_{\rm g,MH}$). The rest-frame J-band (1.2 μm) luminosity $L_{J,{\rm Gal}}$ is used because this is the band closest to 1 μm, and is where the galaxy contribution peaks.

The small photometric errors in J imply that black hole mass measurement errors dominate the error on $f_{\rm g,MH}$. Black hole mass estimates from mass scaling relationships have an error $\Delta M_{\rm BH}/M_{\rm BH} \sim 40$ per cent (Vestergaard & Peterson 2006; Peterson

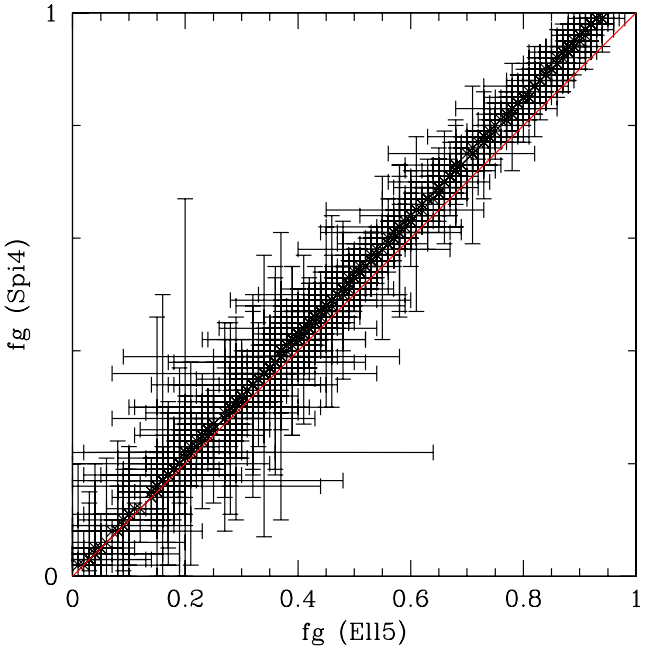

Figure 7. The f_g value of the *XMM*-COSMOS sample using the 5 Gyr elliptical galaxy template (Ell5) and the spiral galaxy (Spi4) from SWIRE template library (Polletta et al. 2007). The red solid line shows the one-to-one relation.

2010), so $\Delta f_{g,MH}/f_{g,MH} \sim 35$ per cent, as $f_{g,MH} \propto M_{BH}^{0.877}$ (according to equation 1).

(2) *Direct imaging*. For 94 low-redshift ($z \lesssim 1.2$) quasars in the *XMM*-COSMOS sample, Cisternas et al. (2011) used the Hubble images to decompose the AGN and galaxy emission and to estimate the host galaxy fraction at 8140 Å (observed frame). We transformed this galaxy fraction to the rest-frame 1 μm galaxy fraction ($f_{g,C}$) using the Ell5 galaxy template. As only the best-fitting model of the host galaxy luminosity is given, we cannot estimate the error on $f_{g,C}$ due to the fitting process.

However, the assumed template introduces an uncertainty. The observed *F*814*W* photometry point lies on the steep side of the galaxy template for $z > 0.1$. Hence, a small error in template slope (or, effectively, in the age of the youngest stellar population in the host) would lead to a large error in the host estimate at 1 μm. We can use this extrapolation uncertainty to estimate a minimum error. To do so, we normalized the 16 SWIRE galaxy templates (Polletta et al. 2007) at 1 μm and measured the dispersion of these different templates at the rest-frame wavelength corresponding to the observed 8140 Å. We use these dispersions as errors on the host galaxy luminosities $L_{g,C}$ at 1 μm for sources at different redshifts. Therefore, the error on the galaxy fraction can be estimated as $\Delta f_{g,C}/f_{g,C} = \Delta L_{g,C}/L_{g,C}$. The error bar ranges from 0.02 to 0.77 with the median value of 0.21.

(3) With the multiwavelength photometry data available, SED fitting can be used to decompose the observed SEDs with some assumptions on the intrinsic component SEDs. Bongiorno et al. (2012) used R06 with SMC-like dust reddening (Prevot et al. 1984), and BC03 models with Calzetti reddening (Calz) to fit the *XMM*-COSMOS sources. We calculate the galaxy fraction and host galaxy luminosity at rest-frame 1 μm from their SED fitting and compare them with the results derived directly from the mixing diagram.

The comparison of f_g estimated from the mixing diagram with the galaxy fraction from the other three methods $f_{g,MH}$ (from Paper I), $f_{g,C}$ (from Cisternas et al. 2011) and $f_{g,B}$ (from Bongiorno et al. 2012) is shown in the top row of Fig. 8. For ease of comparison, we also plot the ratio of the f_g values from the other three methods over f_g from the mixing diagram versus the f_g from mixing diagram in the second row.

The first two methods (scaling relationships and direct imaging decomposition) give values which are poorly correlated with the f_g values from the mixing diagram. The correlation coefficient for f_g and $f_{g,MH}$ is 0.35, for f_g and $f_{g,C}$ is −0.09. $f_{g,MH}$ gives systematically smaller values than the other methods. From equation (1), this effect is either due to a systematic underestimate of black hole mass, or to an overestimate of the evolution of the scaling relationship, which may be more likely (see e.g. Schramm & Silverman 2013).

However, the $f_{g,B}$ values from the SED fitting are strongly correlated with the f_g values from the mixing diagram, although with a shift in normalization. The correlation coefficient between the two sets of values is 0.83. The host galaxy fraction from the SED fitting is systematically slightly higher than the results of the mixing diagram. This is probably due to the galaxy template model employed. The SED fitting in Bongiorno et al. (2012) used BC03 models, which generally have smaller α_{NIR} so the mixing curves are shorter, leading to larger galaxy fractions (see the right-hand panel of Fig. 1).

The inferred 1 μm host galaxy luminosities (L_g, $L_{g,MH}$, $L_{g,C}$ and $L_{g,B}$) are also compared in Fig. 8 (bottom two rows). The correlation coefficient between L_g and $L_{g,MH}$ is 0.17, between L_g and $L_{g,C}$ is 0.33 while that between L_g and $L_{g,B}$ is 0.75. For most cases the inferred host galaxy luminosity νL_ν is less than $10^{44.6}$ erg s^{-1} (that is $M_{1\,\mu m} > -23$), a reasonable value, as $M_K^* \sim -23$ at $0.25 \leq z \leq 1.5$ (Cirasuolo et al. 2007).

Using the mixing diagram to estimate the host galaxy fraction requires the following assumptions: (1) an intrinsic quasar SED exists and is similar to E94 mean SED; (2) the chosen galaxy templates are representative; (3) all the quasars have a similar reddening curve which is SMC like. The first assumption is somewhat reasonable based on the dependence studies of mean SEDs with physical parameters (Paper II) and Section 3.3 in this paper. As shown in Fig. 7, choosing different galaxy templates would give very similar results ($\lesssim 1\sigma$) even for the host-dominated sources. Therefore, the validity of the second assumption will not affect the result much. In practice, one can choose the proper galaxy templates that are closest to the population in discussion or be more careful when citing the f_g for galaxy dominated sources. The reliability of the third assumption is hard to assess. For the currently commonly used extinction curves (SMC, LMC and MW), the difference is small (see Section 4.3).

Estimation of the host galaxy fraction using scaling relationships has a large uncertainty due to the dispersion of the relationship itself (e.g. Marconi & Hunt 2003, Merloni et al. 2010) and possibility of evolution in the relationship (e.g. Merloni et al. 2010, Schramm & Silverman 2013). There are also significant uncertainties of the M_{BH} estimates (Vestergaard & Peterson 2006; Peterson 2010).

Estimates of the host galaxy fraction using image decomposition (e.g. Cisternas et al. 2011) are observationally limited to moderate redshifts. Most importantly, this method leads to large uncertainties, because the ratio of the host galaxy to AGN luminosity is a strong function of the wavelength. The uncertainties of the intrinsic SED shapes in both the host and the quasar will lead to large uncertainty in the fraction if we transfer from the observed wavelength to another wavelength we are interested in (Paper I).

From the mixing diagram we can easily derive the host galaxy fractions at 1 μm and obtain reasonably consistent values with the results from SED fitting (see the rightmost panel of Fig. 8). The

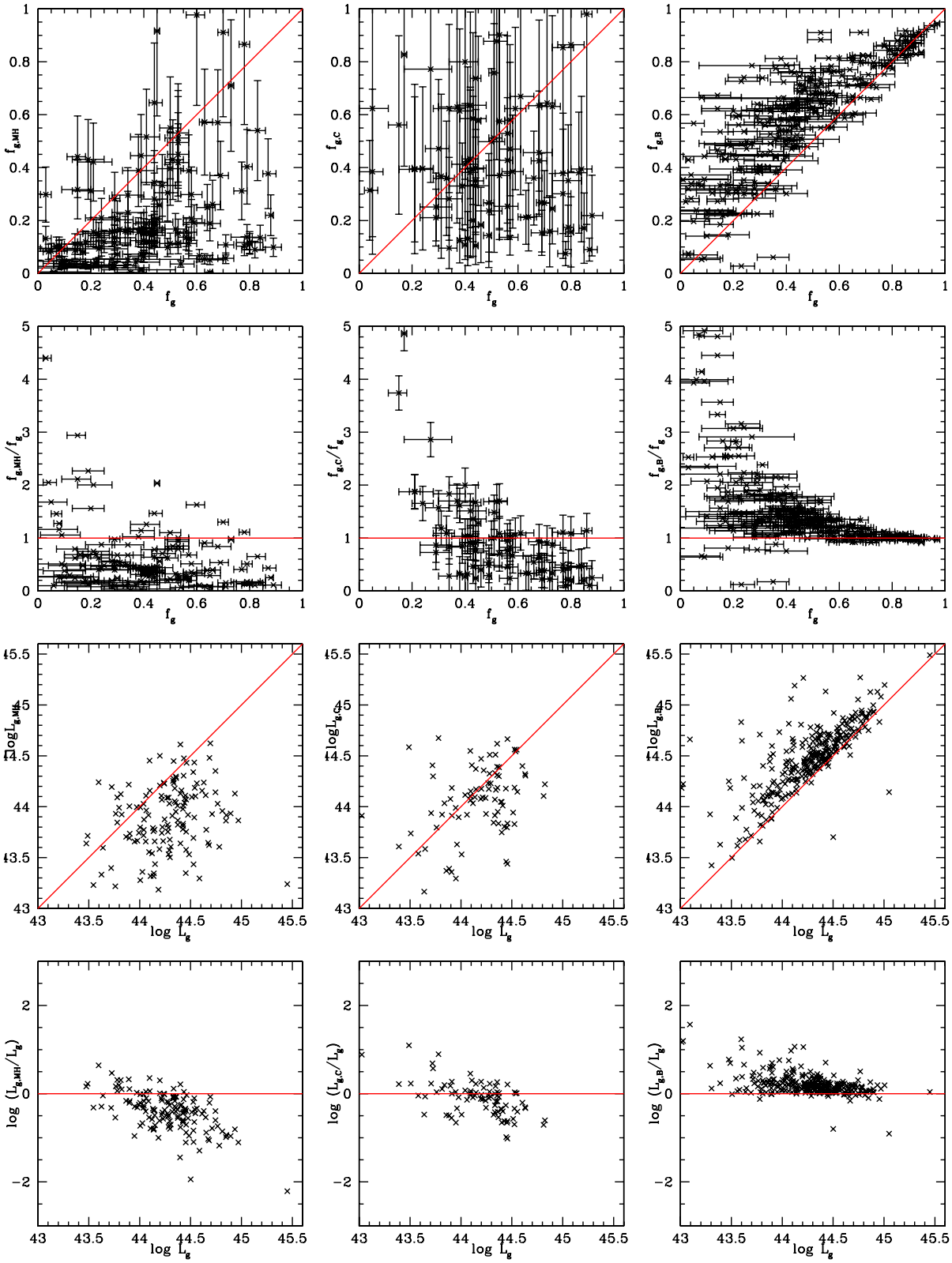

Figure 8. The comparison of the galaxy fraction (top) and host galaxy luminosity (bottom) of the *XMM*-COSMOS sample at rest-frame 1 μm: (1) from the mixing diagram: $f_{\rm g}$, $\log L_{\rm g}$, using Ell5 mixing curve, (2) from the Marconi & Hunt (2003) scaling relationship adding an evolutionary term (Bennert et al. 2010, 2011): $f_{\rm g,MH}$, $\log L_{\rm g,MH}$, (3) from the Hubble image decomposition (Cisternas et al. 2011): $f_{\rm g,\,C}$, $\log L_{\rm g,\,C}$, and (4) from the SED fitting (Bongiorno et al. 2012): $f_{\rm g,\,B}$, $\log L_{\rm g,\,B}$. The red solid lines show the one-to-one relation.

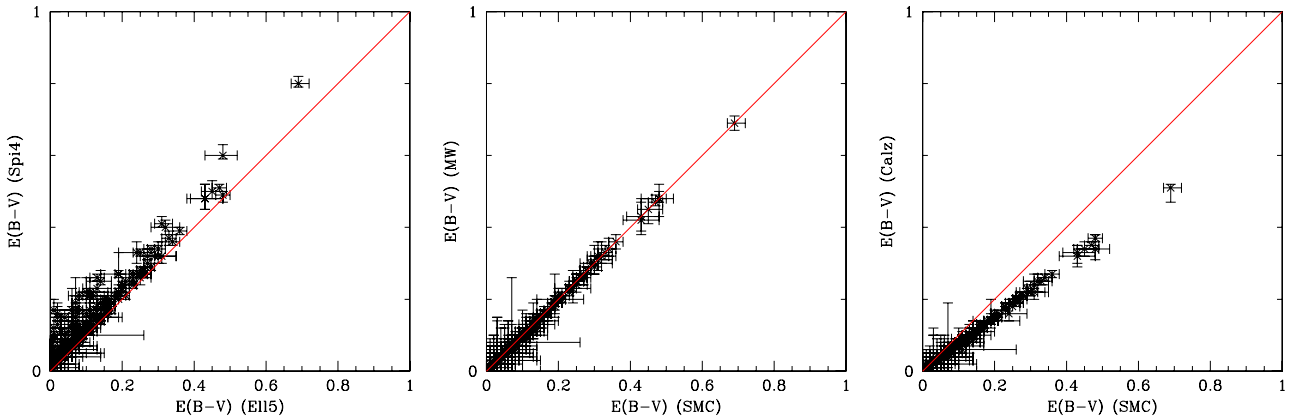

Figure 9. The $E(B-V)$ estimates of the *XMM*-COSMOS sample. (1) Left: using the 5 Gyr elliptical galaxy template (Ell5) and the spiral galaxy (Spi4) from SWIRE template library (Polletta et al. 2007) and using the SMC reddening law for both axis; (2) Centre: using the SMC and MW reddening law, respectively, and using the Ell5 galaxy template for both axis; (3) Right: using the SMC and Calz reddening law, respectively, and using the Ell5 galaxy template for both axis. The red solid line shows the one-to-one relation.

obvious advantage of the use of the mixing diagram is that it is simple to construct and is directly derived from the photometry. The SED fitting uses multiwavelength data over a larger frequency range, but is hard to estimate exactly how the results depend on the number of different components and the assumed component templates.

The f_g calculated from the mixing diagram is thus useful and reliable compared to other methods.

4.3 Inferred reddening

In addition to the galaxy fraction estimation, from the mixing diagram we could get an estimation of the $E(B-V)$ value from the position of the source on the mixing diagram (Section 2.4). The errors on the $E(B-V)$ estimates are also caused by the error on the slopes due to linear fitting of the SEDs similar to the f_g estimates. Different galaxy templates give different f_g values. the left-hand panel of Fig. 9 compares the values $E(B-V)$ for two templates. The correlation coefficient is 0.96 and if a straight line is fitted, the slope is 0.95 ± 0.01, very close to 1. Compared to f_g estimates, the $E(B-V)$ estimates are more affected by which galaxy template is chosen. This is expected as the galaxy templates are distributed in a sparse region on the upper-left part of the mixing diagram. Thus, the mixing curves for different templates would spread out in the large f_g direction, leading to large difference of the $E(B-V)$ estimates for the same quasar.

Different reddening laws used in the mixing diagram will lead to different $E(B-V)$ estimates (middle and right plots of the Fig. 9). As shown in Table 2 and Fig. 1, the SMC and LMC reddening laws lead to the same reddening vector. So there are no differences between the $E(B-V)$ estimates given by these two reddening laws. The MW reddening vector is quite close to the SMC reddening vector leading to similar results in the $E(B-V)$ estimates (centre panel in Fig. 9). The correlation coefficient between the SMC and MW $E(B-V)$ values is 0.999. If a line is fitted, the slope is 0.99 ± 0.02 and the intersection is 0.0002. So the SMC, LMC and MW reddening laws give the same $E(B-V)$ estimates. The $E(B-V)$ estimates derived from the Calz reddening law are different, especially for large $E(B-V)$. However, when compared to results from the SMC law (right-hand panel of Fig. 9), the correlation coefficient is 0.998 and the slope is 0.74 ± 0.02. The estimates of $E(B-V)$ derived from different reddening laws are all tightly correlated.

$E(B-V)$ is estimated by applying a standard extinction law to an assumed intrinsic OPT-to-NIR quasar SED template (e.g. Vasudevan et al. 2009; Glikman et al. 2012). Here, the SMC extinction curve is chosen because the extinction curve of quasars is generally believed to be better described by the SMC type (Hopkins et al. 2004; Gallerani et al. 2010). The $E(B-V)$ estimate derived from the mixing diagram is equivalent to assuming the E94 template as an intrinsic quasar template and applying the SMC reddening law. As the E94 template is the mean SED of the bright quasar sample, and for each quasar in the E94 sample the possible reddening is not corrected, we expect the E94 template to be slightly redder than the intrinsic quasar SED. In this case, the $E(B-V)$ estimation derived from the mixing diagram should be a lower limit. As a fraction of the quasars lies in the upper-right corner beyond the mixing curve leading to negative $E(B-V)$ values, we ignore these quasars from further discussion in this section. If different galaxy templates with younger stellar populations are chosen, these sources could lie within the mixing region with positive $E(B-V)$ estimates. The size of the galaxy fraction clearly depends on the mixing curve chosen to derive the $E(B-V)$ values.

Other than estimate the $E(B-V)$ from the OPT-to-NIR SED, Balmer decrements have been used historically to estimate the reddening along the line of sight of quasars (e.g. Maiolino et al. 2001; Xiao et al. 2012). However, this method requires spectra that include both the Hα and Hβ lines, which is not suitable for the *XMM*-COSMOS sample, because most of the quasars are at redshifts around 1–2. Besides, Glikman et al. (2012) argued that using the OPT-to-NIR SED to estimate the reddening is much more reliable than the Balmer decrements estimation.

Other independent estimates of $E(B-V)$ are very difficult. The galaxy inclination derived from *HST* images or the total dust masses estimated from the infrared luminosity might give a hint to how much reddening we would expect, but to get $E(B-V)$ estimates by these methods would require lots of assumption on the gas and dust content of the host galaxy. Thus, it is very difficult to compare the $E(B-V)$ values derived from the mixing diagram with those from other measurements to test the reliability of the mixing diagram. In general, we would expect that for quasars with high $E(B-V)$ values, the infrared bump would be more prominent and the 'big-blue-bump' would be less prominent. We check the correlation of the NIR luminosity fraction (L_{ir}/L_{bol}, where L_{ir} is the luminosity integrated from rest-frame 24 μm to 1 μm; Paper II) and the OPT luminosity

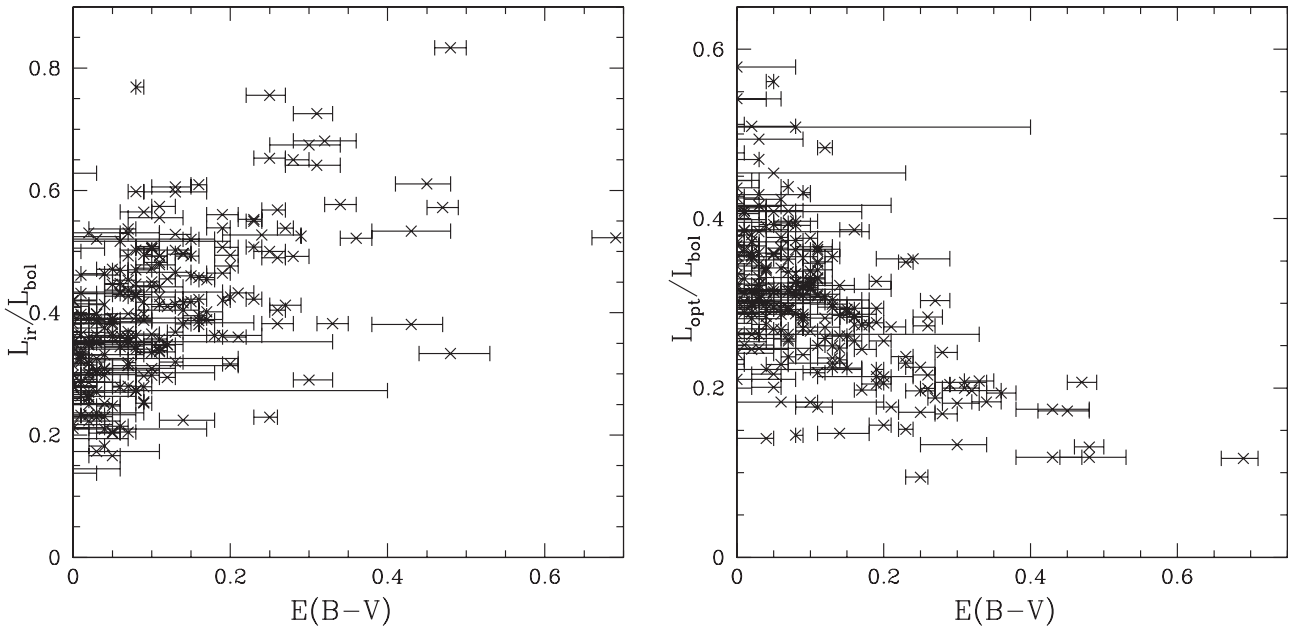

Figure 10. The NIR luminosity fraction versus $E(B-V)$ (left) and the OPT luminosity fraction versus $E(B-V)$ (right). Here, we use the 5 Gyr elliptical galaxy template (Ell5) from SWIRE template library (Polletta et al. 2007) and the SMC reddening law to derive the $E(B-V)$ estimates.

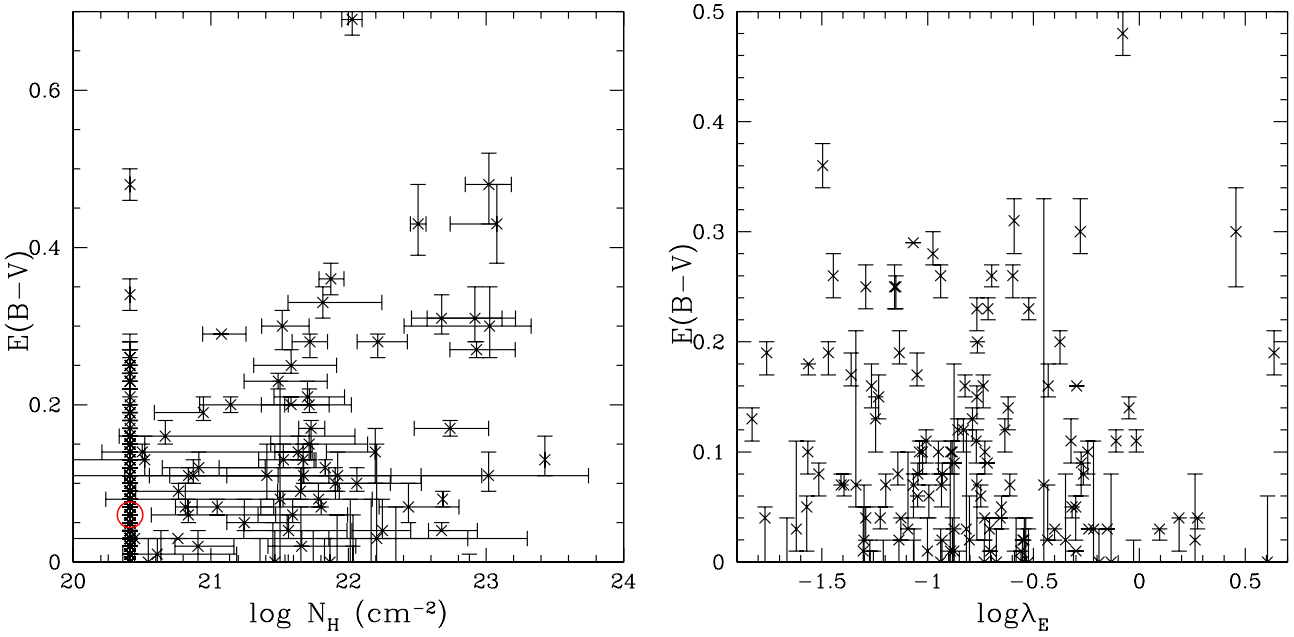

Figure 11. $E(B-V)$ versus the neutral Hydrogen column density N_H (left) and $E(B-V)$ versus Eddington ratio $\log\lambda_E = \log(L_{bol}/L_{Edd})$ (right). Here, we use the 5 Gyr elliptical galaxy template (Ell5) from SWIRE template library (Polletta et al. 2007) and the SMC reddening law to get the $E(B-V)$ estimates. The red circle in the left-hand panel shows the median $E(B-V)$(=0.06) of the AGN with no intrinsic N_H.

fraction (L_{opt}/L_{bol}, where L_{opt} is the luminosity integrated from rest-frame 1 μm to 912 Å; Paper II) with $E(B-V)$, respectively (Fig. 10). In Fig. 10, we compare the OPT and NIR luminosity fraction with the $E(B-V)$ values derived from the Ell5 mixing curve as an example. For the 226 quasars with positive $E(B-V)$ values from the Ell5 mixing curve, the correlation coefficient for the NIR luminosity fraction with $E(B-V)$ is 0.54 and for the OPT luminosity fraction with $E(B-V)$ is −0.62. So the OPT and NIR luminosity fractions with $E(B-V)$ are correlated as expected.

The neutral hydrogen column density (N_H) estimated from the X-ray spectrum is usually used as an indicator of the absorber. However, the OPT and X-ray obscuration are caused by different physical processes and thus can be very different in an object (e.g. Crenshaw & Kraemer 2001). We compare the estimated $E(B-V)$ values from mixing diagram with the X-ray N_H values (Mainieri et al. 2007) for the *XMM*-COSMOS sample (Fig. 11, left). For the 413 quasars in *XMM*-COSMOS sample, 378 quasars have good enough *XMM* spectra to make a fit. In 273 out of the 378 cases, no intrinsic N_H is necessary from the spectrum, so the N_H value is set to the Galactic N_H in the COSMOS region ($\log N_H = 20.413\,cm^{-2}$). Using the 205 quasars with an N_H estimate and positive $E(B-V)$ give a correlation coefficient of 0.40, which corresponds to a significant correlation

at $>5\sigma$ level. Fig. 11 (left) shows a clear correlation with some potentially interesting outliers, e.g. objects with no intrinsic $N_{\rm H}$ and high $E(B-V)$.

Low accretion rate (Eddington ratio $\lambda_{\rm E} \lesssim 10^{-4}$) quasars are thought to have more reddened 'big-blue-bump' (e.g. Ho 2008; Trump et al. 2011). We compare the estimated $E(B-V)$ versus the Eddington ratio ($\lambda_{\rm E}$) in Fig. 11 (right) to see if there is a similar trend in *XMM*-COSMOS sample. The correlation coefficient between $E(B-V)$ and $\log\lambda_{\rm E}$ is -0.035 for the 119 quasars with $\log\lambda_{\rm E}$ estimates and positive $E(B-V)$ estimates, thus no correlation is observed. The studies of Fabian, Vasudevan & Gandhi (2008) and Fabian et al. (2009) identify the effective Eddington limit for dusty gas in the $N_{\rm H}-\lambda_{\rm E}$ plane, and therefore causing a 'forbidden region' in the $N_{\rm H}-\lambda_{\rm E}$ space within which absorbing dusty gas clouds are unstable to radiation. Vasudevan et al. (2009) show a similar 'forbidden region' in the upper-right corner of the $E(B-V)-\lambda_{\rm E}$ plane. In the right-hand panel of Fig. 11, we can see a similar lack of high accretion rate and high $E(B-V)$ objects.

4.4 Mixing diagram outliers

There are sources lying outside the mixing wedge that are outliers with respect to the bulk of the type 1 AGN population. As noted above (Section 4.1), the mixing diagram has already been successfully used to identify a population of HDP quasars lacking the characteristic maximally hot dust of AGN (Hao et al. 2010, 2011).

The four extreme examples of SEDs singled out in Paper I (A, B, C, D) are also marked in Fig. 2. They lie at the four corners of the mixing diagram. Fig. 12 displays the SEDs of four additional outliers (E, F, G, H) which are discussed briefly below. These four quasars lies in the furthest corners of the mixing diagram. A detailed discussion will be deferred to later papers.

(i) *A newborn quasar?* Object E (XID = 304, COSMOS J095931.58+021905.52, $z = 1.607$) has an SED well fit by the ULIRG Arp 220 SED (Polletta et al. 2007) at $\lambda > 0.40\,\mu$m. However, in the UV (at $\lambda < 0.40\,\mu$m), a weak quasar component emerges, as do the BELs that identify it as a type 1 AGN. This object has a luminosity in the ULIRG regime (the bolometric luminosity integrated in 24 μm–40 keV range is $10^{12.2}\,{\rm L}_{\odot}$) and appears to be a composite quasar/starburst. The rarity of objects like E in *XMM*-COSMOS argues for a short-lived phase. Object E is thus a good candidate for a newly born quasar, or at the beginning of the 'buried quasar stage', where the quasar emerges during a merger-triggered starburst (Hopkins et al. 2006). The obscured starburst activity still dominates the SED and the quasar is still too weak to quench the starburst activity.

(ii) *A weak big blue bump quasar?* Object F (XID = 135, COSMOS J095848.21+022409.3, $z = 0.376$) shows a 2 dex drop in the u band compared to the E94 RQ mean SED. An extinction of $E(B-V) = 0.8$ could be applied. This source is classified as type 1 AGN because a strong broad Hα line (FWHM $\sim 5000\,{\rm km\,s^{-1}}$) is present in the OPT spectrum. There may be strong differential reddening between the continuum and the broad-line emitting region. Alternatively, an NGC 6090 template fits the OPT/UV SED well. Is then the UV 'big blue bump' intrinsically weak in this object? The high X-ray flux relative to the OPT would make for a truly unusual SED in the extreme UV.

(iii) *A 'blow-out' phase quasar?* Object G (XID = 5607, COSMOS J095743.33+024823.8, $z = 1.359$) is well fitted by the E94 RQ mean SED in the OPT/UV, but shows an unusually strong NIR bump, two times brighter than the E94 RQ mean SED at 3 μm, indicating an unusually rich hot dust component. Such a quasar could be a good candidate for objects at the end of the 'buried quasar stage' or the beginning of the 'blow-out phase', where the quasar emerges from its dusty cocoon and begins to dominate the SED (Hopkins et al. 2006). The properties of these quasars still need to be investigated.

(iv) *HDP quasar.* Object H (XID = 504, COSMOS J095931.01+021333.0, $z = 3.651$) is located in the upper-right corner, furthest from the E94 mean SED template in the mixing diagram of the XC413 sample. The SED of object H has a typical strong big blue bump but weak infrared emission. It is another HDP quasar, similar to source D described in Paper I, and discussed in detail in Hao et al. (2010). These could be sources that have used up or blown-out most their dust and gas.

5 DISCUSSION AND CONCLUSIONS

Making use of the strong SED shape differences around 1 μm for galaxies and quasars, we defined the quasar–galaxy mixing diagram: a plot of the 1–3 μm SED slope versus the 0.3–1 μm SED slope. This diagram allows us to easily distinguish among quasar-dominated, galaxy-dominated and reddening-dominated SEDs without making strong model assumptions.

This mixing diagram, when applied to the *XMM*-COSMOS sample shows that ∼90 per cent of the quasar SEDs can be explained by the combination of (1) an E94-like mean SED, (2) a host galaxy SED and (3) reddening. The mixing diagram is a very useful tool and, as we have outlined, has various applications.

Changes in the quasar SED shape with respect to the physical parameters z, $L_{\rm bol}$, $M_{\rm BH}$ and $\lambda_{\rm E}$ were sought. At high z, $\log L_{\rm bol}$, $\log M_{\rm BH}$ and $\log\lambda_{\rm E}$, the *XMM*-COSMOS quasars cluster close to the E94 mean, with a slight offset, which could be due to either an intrinsic SED change, or a small but not negligible host galaxy component. Lower z, $L_{\rm bol}$, $M_{\rm BH}$ and $\lambda_{\rm E}$ sources spread along the E94 mean SED–host mixing curves. The mixing diagram allows estimates of the galaxy fraction and the reddening for each AGN. Reddening of $E(B-V) > 0.4$ is seen mainly among low z, $L_{\rm bol}$ objects.

Most importantly, the mixing diagram can give a reliable estimate of the 1 μm host galaxy fraction or luminosity and the $E(B-V)$. The galaxy fractions estimated from the mixing diagram were compared with those estimated from the black hole mass–bulge mass scaling relationship adding an evolutionary term, from direct Hubble image decomposition and from SED fitting. The host fraction estimated from the scaling relationship and the image decomposition show weak correlation with the galaxy fraction from the mixing diagram, though all have large errors. The black hole mass–bulge method gives systematically smaller galaxy fractions. But the galaxy fractions from the mixing diagram are consistent with the results from the SED fitting. The mixing diagram appears to be a useful and reliable tool to estimate the host galaxy fraction and luminosity at 1 μm.

The reddening [$E(B-V)$] estimated from the mixing diagram were correlated with the NIR luminosity ratio ($L_{\rm ir}/L_{\rm bol}$) and OPT luminosity ratio ($L_{\rm opt}/L_{\rm bol}$). A significant correlation is found for $E(B-V)$ versus $N_{\rm H}$, although with a large spread. The derived $E(B-V)$ and $\lambda_{\rm E}$ are not significantly correlated. A 'forbidden region' in the $E(B-V)$ versus $\lambda_{\rm E}$ space is seen as in Vasudevan et al. (2009).

The mixing diagram can be used also to identify outliers. As these AGN are rare in a deep X-ray selected sample, they may represent different short-lived stages of the quasar–galaxy co-evolution.

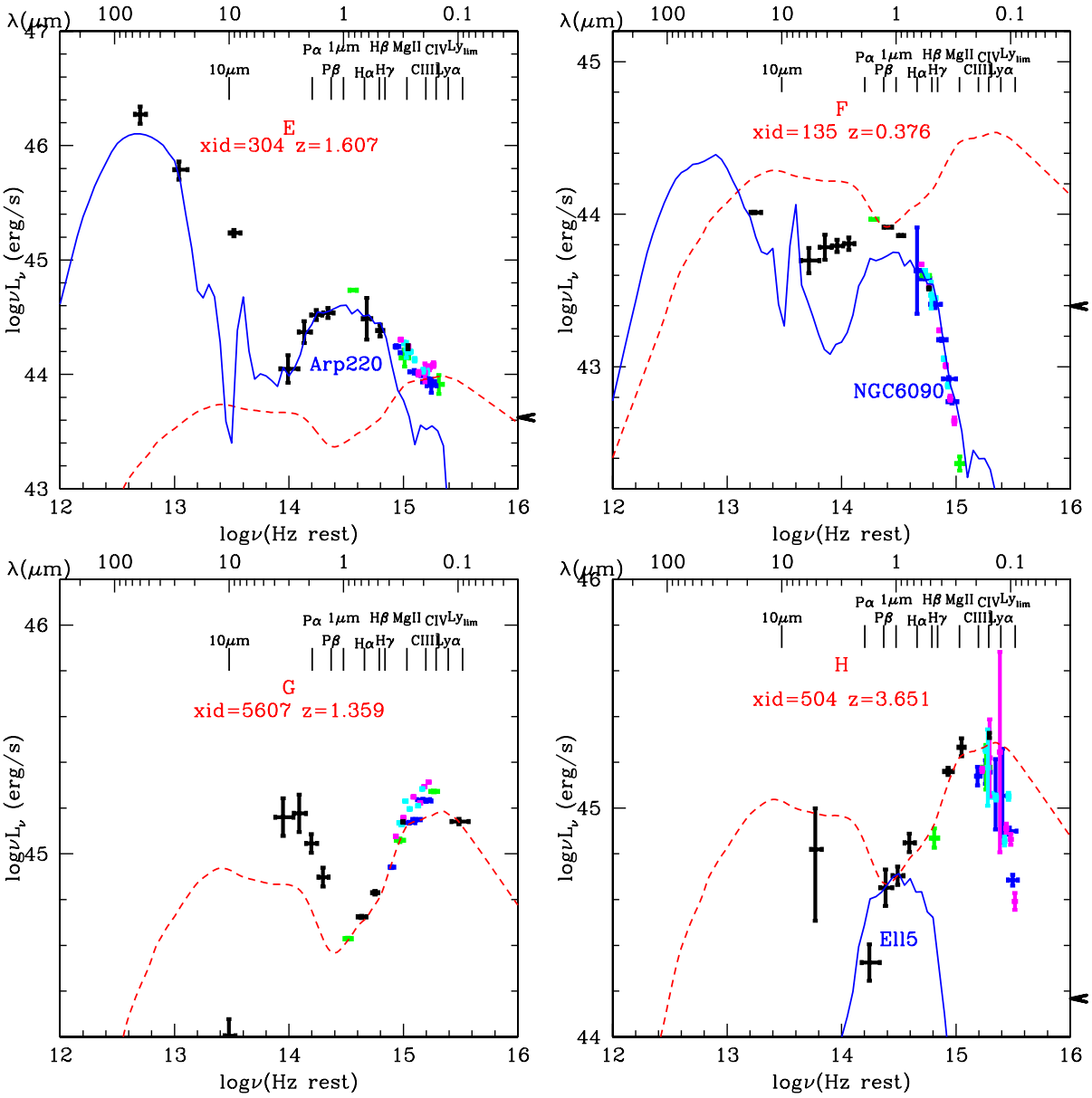

Figure 12. Extreme examples of SEDs. Top left: E – a close analogue of a ULIRG SED, with prominent infrared emission; top right: F – no big blue bump, probably due to extreme reddening; bottom left: G – big NIR bump, due to rich hot dust emission; bottom right: H – HDP quasar, strong big blue bump but no 1 μm inflection due to a weak NIR bump. The red dashed line is the E94 RQ mean SED. The blue lines are the galaxy templates (Polletta et al. 2007). The data points in the SED are colour-coded as in Paper I. From low frequency to high frequency, the black data points are: 24, 8, 5.7, 4.5, 3.6, *K* band, *H* band, *J* band, the NUV and FUV. The blue data points are the Subaru broad-bands (B_J, *g*, *r*, *i*, *z*) from 2005. The green data points are the (CFHT) *K* band, and the (CFHT) *u* band and *i* band. The purple data points are the six Subaru intermediate bands for season 1 (2006) (IA427, IA464, IA505, IA574, IA709, IA827). The cyan data points are the five Subaru intermediate bands for season 2 (2007) (IA484, IA527, IA624, IA679, IA738, IA767). The arrow on the right show the X-ray luminosity at 2 keV.

The mixing diagram can clearly distinguish among the quasar-dominated, host-dominated and reddening-dominated SEDs. Thus different phases of galaxy formation and evolution would locate in different regions of the diagram. A complete evolutionary track of the quasar–galaxy co-evolution cycle can, in principle, be drawn on the mixing diagram, by analogy to tracks in the Hertzsprung-Russell diagram in stellar astrophysics. Numerical simulations have reproduced quasars at various redshifts from hierarchical assembly in the Λ cold dark matter cosmology (Hopkins et al. 2006; Li et al. 2007), but have not addressed how the resulting SEDs change.

There are various different galaxy formation and evolution models. Two representatives would be (1) the 'cosmic cycle' (Hopkins et al. 2006) for galaxy formation and evolution, which are regulated by black hole growth in mergers; and (2) the galaxy evolution triggered by self-regulated baryonic process (Granato et al. 2004). The main difference between these two models is in the beginning phase: (1) in the merger-driven model (Hopkins et al. 2006), star formation is enhanced by the merging of two late-type galaxies; (2) in the antihierarchical baryon collapse model (Granato et al. 2004) the protospheroidal galaxies formed in the virialized dark matter halo have high star formation rate (Mao et al. 2007; Cai et al. 2013).

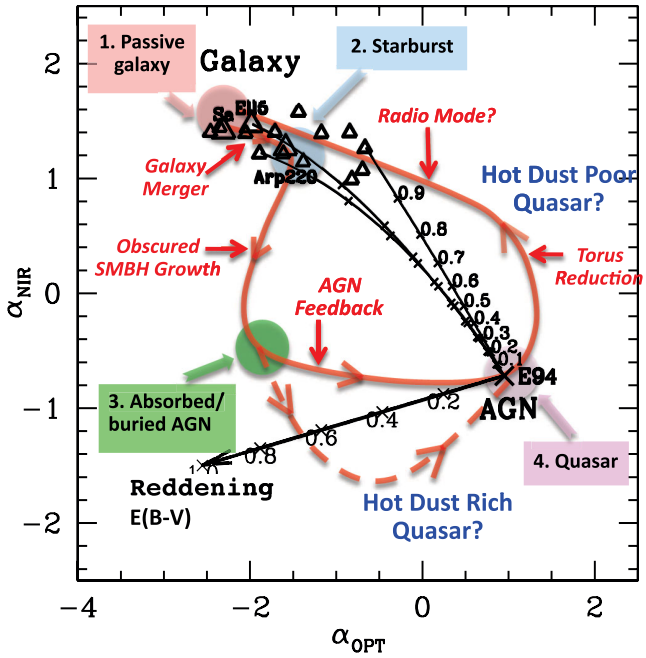

Figure 13. The evolution view of the mixing diagram. Four different phases of the 'cosmic cycle' are shown as coloured circles. The red line shows the evolution track of an AGN life cycle.

The following black hole growth (Lapi et al. 2006; Hopkins et al. 2006) and galaxy evolution in both models are similar to each other with some difference in time-scales of different phases. Thus in the mixing diagram, the evolutionary tracks between different models would be very similar in most regions.

A sketch of a possible evolutionary track is shown in Fig. 13. Mergers drive a galaxy (1, red) into the starburst region (2, blue). Here, the SMBH grows by accretion. The quasar emission gradually comes to dominate the luminosity, but is 'buried' by gas and dust, so the source moves downwards in the mixing diagram for the phase of obscured quasar activity (3, green). Sources in this stage would be identified as type 2 AGN, not included in the XC413 sample. At the end of this buried quasar phase, hot dust rich (HDR) quasars – the outliers with much stronger hot dust emission than typical quasar and BELs – would be found at the very bottom of the mixing diagram. At this stage, feedback from the SMBH expels enough interstellar medium, and the obscuring 'torus' and the broad-line region emission become visible, and the object gradually moves either from a 'buried' or 'HDR' quasar to the typical quasar region (4, purple) if the ratio between AGN and host galaxy luminosity is high. Lower luminosity AGN would move near the mixing curves. As the SMBH continues to accrete, the gas and dust is either used up as a reservoir, or expelled. The dust covering factor reduces, and the source moves up to the HDP quasar region, before finally becoming quiescent once more. The length of the time-scale of each stage may be reflected by the number of sources in each region on the mixing diagram in a complete sample.

A family of possible evolutionary cycles could be drawn, varying the parameters of the initial merging (e.g. mass, gas fraction, accretion rate). A quantitative picture of the cosmic cycle (e.g. the duration of the duty cycle in each phase, the dependence on the initial conditions, etc.) could thus be obtained from the density of objects around the mixing diagram. These results, in turn, could put constraints on the physics adopted to model AGN/galaxy co-evolution in numerical simulations. We will address the quantitative evolution of quasar–galaxy SEDs in the mixing diagram, over the complete cosmic cycle in later papers, including also the analysis of type 2 AGN.

However, we have to note that Fig. 13 is just an idealized illustration. The tracks of the evolution of sources could be very complicated and sources could evolve in various direction in the mixing region. Bongiorno et al. (2012) plotted all the *XMM*-COSMOS sources in the mixing diagram and there is no obvious accretion rate distribution correlated with different regions on the mixing diagram observed.

For a longer term study of the full evolutionary picture, the mixing diagram definition could be extended to other wavelengths. For example, we could investigate the OPT to ultraviolet SED with respect to the NIR SED for the extinction law; we could study the radio and far-infrared SED with respect to OPT/NIR for the radio-loudness; we could check the ultraviolet SED with respect to X-ray for the α_{OX}. The multiwavelength analysis of the AGN emission could not only significantly improve our understanding of the SMBH accretion, the AGN structure and the unification of AGN, but also would help us understand the role of the SMBH in the co-evolution cosmic cycle.

ACKNOWLEDGEMENTS

HH thanks Belinda Wilkes, Martin J. Ward and Zhenyi Cai for valuable discussions. This work was supported in part by NASA *Chandra* grant number G07-8136A (HH, ME, CV). Support from the Italian Space Agency (ASI) under the contracts ASI-INAF I/088/06/0 and I/009/10/0 is acknowledged (AC and CV). MS acknowledges support by the German Deutsche Forschungsgemeinschaft, DFG Leibniz Prize (FKZ HA 1850/28-1). KS gratefully acknowledges support from Swiss National Science Foundation Grant PP00P2_138979/1.

REFERENCES

Alongi M., Bertelli G., Bressan A., Chiosi C., Fagotto F., Greggio L., Nasi E., 1993, A&AS, 97, 851
Barvainis R., 1987, ApJ, 320, 537
Bennert V. N., Treu T., Woo J.-H., Malkan M. A., Le Bris A., Auger M. W., Gallagher S., Blandford R. D., 2010, ApJ, 708, 1507
Bennert V. N., Auger M. W., Treu T., Woo J.-H., Malkan M. A., 2011, ApJ, 742, 107
Bongiorno A. et al., 2007, A&A, 472, 443
Bongiorno A. et al., 2012, MNRAS, 427, 3103
Bouwens R. J. et al., 2012, ApJ, 754, 83
Brandt W. N., Hasinger G., 2005, ARA&A, 43, 827
Bressan A., Fagotto F., Bertelli G., Chiosi C., 1993, A&AS, 100, 647
Brusa M. et al., 2007, ApJS, 2007, 172, 353
Brusa M. et al., 2010, ApJ, 716, 348
Bruzual G., Charlot S., 2003, MNRAS, 344, 1000 (BC03)
Cai Z. et al., 2013, ApJ, 768, 21
Calzetti D., Armus L., Bohlin R. C., Kinney A. L., Koornneef J., Storchi-Bergmann T., 2000, ApJ, 533, 682 (Calz)
Capak P. et al., 2007, ApJS, 172, 99
Cappelluti N. et al., 2007, ApJS, 172, 341
Cappelluti N. et al., 2009, A&A, 497, 635
Cardelli J. A., Clayton G. C., Mathis J. S., 1989, ApJ, 345, 245
Chabrier G., 2003, PASP, 115, 763
Cirasuolo M. et al., 2007, MNRAS, 380, 585
Cisternas M. et al., 2011, ApJ, 726, 57
Civano F. et al., 2011, ApJ, 741, 91
Coleman G. D., Wu C. C., Weedman D. W., 1980, ApJS, 43, 393
Crenshaw D. M., Kraemer S. B., 2001, ApJ, 562, L29

Elvis M. et al., 1994, ApJS, 95, 1 (E94)
Elvis M. et al., 2012, ApJ, 759, 6 (Paper I)
Fabian A. C., Vasudevan R. V., Gandhi P., 2008, MNRAS, 385, L43
Fabian A. C., Vasudevan R. V., Mushotzky R. F., Winter L. M., Reynolds C. S., 2009, MNRAS, 394, 89
Fagotto F., Bressan A., Bertelli G., Chiosi C., 1994a, A&AS, 104, 365
Fagotto F., Bressan A., Bertelli G., Chiosi C., 1994b, A&AS, 105, 29
Ferrarese L., Merritt D., 2000, ApJ, 539, L9
Fitzpatrick E. L., 1999, PASP, 111, 63
Franceschini A., Hasinger G., Miyaji T., Malquori D., 1999, MNRAS, 310, L5
Gallerani S. et al., 2010, A&A, 523, 85
Gebhardt K. et al., 2000, AJ, 539, L13
Girardi L., Bressan A., Chiosi C., Bertelli G., Nasi E., 1996, A&AS, 117, 113
Glikman E., Helfand D. J., White R. L., 2006, ApJ, 640, 579
Glikman E. et al., 2012, ApJ, 757, 51
Gordon K., Clayton G. C., Misselt K. A., Landolt A. U., Wolf M. J., 2003, ApJ, 594, 279
Granato G. L., De Zotti G., Silva L., Bressan A., Danese L., 2004, ApJ, 600, 580
Hao H. et al., 2010, ApJ, 724, L59
Hao H., Elvis M., Civano F., Lawrence A., 2011, ApJ, 733, 108
Hao H. et al., 2013a, MNRAS, preprint (arXiv:1210.3033) (Paper II)
Hao H. et al., 2013b, ApJ, submitted
Hasinger G. et al., 2007, ApJS, 172, 29
Ho L. C., 2008, ARA&A, 46, 475
Hopkins P. F. et al., 2004, AJ, 128, 1112
Hopkins P. F., Hernquist L., Cox T. J., Di Matteo T., Robertson B., Springel V., 2006, ApJS, 163, 1
Hopkins P. F., Richards G. T., Hernquist L., 2007, ApJ, 654, 731
Ilbert O. et al., 2009, ApJ, 690, 1236
Ilbert O. et al., 2010, ApJ, 709, 644
Jiang L. et al., 2010, Nat, 464, 380
Kelly B. C., 2007, ApJ, 665, 1489
Kewley L. J., Groves B., Kauffmann G., Heckman T., 2006, MNRAS, 372, 961
Komatsu E. et al., 2009, ApJS, 180, 330
Kormendy J., Richstone D., 1995, ARA&A, 33, 581
Lapi A., Shankar F., Mao J., Granato G. L., Silva L., De Zotti G., Danese L., 2006, ApJ, 650, 42
Li Y. et al., 2007, ApJ, 665, 187
Lilly S. J. et al., 2007, ApJS, 172, 70
Lilly S. J. et al., 2009, ApJS, 184, 218
Mainieri V. et al., 2007, ApJS, 172, 368
Maiolino R., Marconi A., Salvati M., Risaliti G., Severgnini P., Oliva E., La Franca F., Vanzi L., 2001, A&A, 365, 28
Malkan M. A., Sargent W. L. W., 1982, ApJ, 254, 22
Mao J., Lapi A., Granato G. L., De Zotti G., Danese L., 2007, ApJ, 667, 655
Marconi A., Hunt L. K., 2003, ApJ, 589, L21
McCracken H. J. et al., 2010, ApJ, 708, 202
McLure R. J., Jarvis M. J., 2002, MNRAS, 337, 109
Merloni A., Heinz S., 2012, in Keel W., ed., Planets, Stars and Stellar Systems, Vol. 6. Springer
Merloni A. et al., 2010, ApJ, 708, 137
Misselt K. A., Clayton G. C., Gordon K. D., 1999, ApJ, 515, 128
O'Brien P. T., Wilson R., Gondhalekar P. M., 1988, MNRAS, 233, 801
O'Donnell J. E., 1994, ApJ, 422, 158
Peterson B. M., 2010, in Peterson B., Somerville R., Storchi-Bergmann T., eds, Proc. IAU Symp. 267, Co-evolution of Central Black Holes and Galaxies. Cambridge Univ. Press, Cambridge, p. 151
Polletta M. et al., 2007, ApJ, 663, 81
Prevot M. L., Lequeux J., Prevot L., Maurice E., Rocca-Volmerange B., 1984, A&A, 132, 389
Richards G. T. et al., 2003, AJ, 126, 1131
Richards G. T. et al., 2006, ApJS, 166, 470 (R06)
Salvato M. et al., 2009, ApJ, 690, 1250
Sandage A., 1971, in O'Connell D. J. K., ed., Proc. Study Week on Nuclei of Galaxies, Pontificiae Academiae Scientiarum Scripta Varia. North Holland, Amsterdam, p. 271
Sanders D. B., Phinney E. S., Neugebauer G., Soifer B. T., Matthews K., 1989, ApJ, 347, 29
Schawinski K., Virani S., Simmons B., Urry C. M., Treister E., Kaviraj S., Kushkuley B., 2009, ApJ, 692, L19
Schmidt M., Green R. F., 1983, ApJ, 269, 352
Schneider D. P. et al., 2007, AJ, 134, 102
Schramm M., Silverman J. D., 2013, ApJ, 767, 13
Scoville N. Z. et al., 2007, ApJS, 172, 1
Shang Z. et al., 2011, ApJS, 196, 2
Sikora M., Stawarz L., Lasota J. P., 2007, ApJ, 658, 815
Silverman J. D. et al., 2005, ApJ, 624, 630
Soltan A., 1982, MNRAS, 200, 115
Trump J. R. et al., 2009, ApJ, 696, 1195
Trump J. R. et al., 2011, ApJ, 733, 60
Ueda Y., Akiyama M., Ohta K., Miyaji T., 2003, ApJ, 598, 886
Vanden Berk D. E. et al., 2001, AJ, 122, 549
Vasudevan R. V., Mushotzky R. F., Winter L. M., Fabian A. C., 2009, MNRAS, 399, 1553
Vestergaard M., 2004, ApJ, 601, 676
Vestergaard M., Peterson B. M., 2006, ApJ, 641, 689
Ward M., Elvis M., Fabbiano G., Carleton N. P., Willner S. P., Lawrence A., 1987, ApJ, 315, 74
Weedman D., 1973, ApJ, 183, 29
Wild V., Heckman T., Charlot S., 2010, MNRAS, 405, 933
Wills B. J., Netzer H., Wills D., 1985, ApJ, 288, 94
Xiao T., Wang T., Wang H., Zhou H., Lu H., Dong X., 2012, MNRAS, 421, 486
Young M., Elvis M., Risaliti G., 2008, ApJ, 688, 128

SUPPORTING INFORMATION

Additional Supporting Information may be found in the online version of this article:

Table 1. Spectral slopes for different f_g values (mixing curve) assuming E94 mean SED as the pure quasar SED (http://mnras.oxfordjournals.org/lookup/suppl/doi:10.1093/mnras/stt1228/-/DC1).

Please note: Oxford University Press are not responsible for the content or functionality of any supporting materials supplied by the authors. Any queries (other than missing material) should be directed to the corresponding author for the article.

This paper has been typeset from a TEX/LATEX file prepared by the author.